Chair of Functional Materials and Materials Systems

Master's Thesis

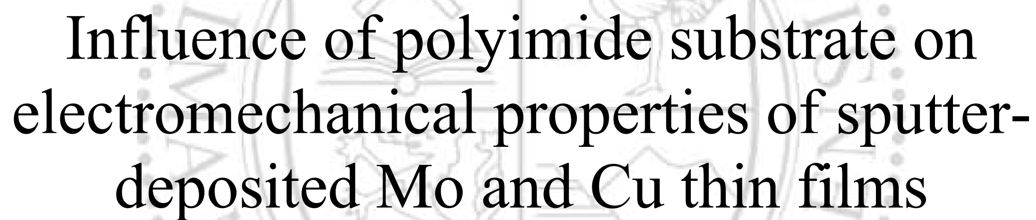

Influence of polyimide substrate on electromechanical properties of sputter-deposited Mo and Cu thin films

Lukas Sebastian Haiden, BSc

May 2020

AFFIDAVIT

I declare on oath that I wrote this thesis independently, did not use other than the specified sources and aids, and did not otherwise use any unauthorized aids.

I declare that I have read, understood, and complied with the guidelines of the senate of the Montanuniversität Leoben for "Good Scientific Practice".

Furthermore, I declare that the electronic and printed version of the submitted thesis are identical, both, formally and with regard to content.

Date 28.05.2020

Haiden Lukas

Signature Author
Lukas Sebastian, Haiden

Acknowledgment

I would like to express my gratitude to Univ.-Prof. DI Dr. Christian Mitterer, who gave me the opportunity to write my master's thesis at the Chair of Functional Materials and Materials Systems and to work in the field of thin films.

A big thank you to my supervisor Dr. Robert Franz for his advice and input he gave me while planning and conducting the experiments and his great patience during the correction of this thesis.

Many thanks to Priv.Doz. Dr. Megan J. Cordill and Dr. Oleksandr Glushko for their help and suggestions for improvement during the execution of the experiments and always having an open ear for my problems.

I would also like to thank Sabrina Hirn and Isabella Eichbauer for helping me producing the thin films for the thesis, DI Patrice Kreiml for introducing me to the confocal laser microscope and DI Ao Xia for his help with the evaluation of the test results. Thank you for your friendship.

Special thanks to DI Dr. Michael Feuchter of the Chair of Materials Science and Testing of Polymers for his assistance at conducting the Differential Scanning Calorimetry measurements.

Furthermore, I want to say thank you to all my colleagues at the Chair of Functional Materials and Materials Systems for helping me at any time and the interesting discussions we had together.
A huge thank to all my friends who were supportive during my whole study time and did make it special.

My final thanks go to my family, especially my parents who always gave me confidence and support in any bad times and the strength to achieve my goals.

Content

1 Introduction 1

2 Theoretical Background 3

2.1 Physical Vapour Deposition 3

2.1.1 Sputter Deposition 3

2.1.2 DC Magnetron Sputtering 4

2.1.3 High-Power Impulse Magnetron Sputtering 6

2.1.4 Sputter Yield 7

2.1.5 Structure Zone Models 8

2.2 X-ray Diffraction 10

2.3 Differential Scanning Calorimetry 13

2.4 In-situ 4-Point Probe Measurement 14

2.5 Optical in situ measurements 16

2.6 Polyimides 18

3 Experimental Details 20

3.1 Film Deposition 20

3.2 Substrate Characterization 24

3.3 Film Characterization 24

4 Results and Discussion 27

4.1 Properties of Polyimide Substrates 27

4.2 Thin Film Structure 29

4.3 Electromechanical Behaviour of the Thin Films 31

4.3.1 Mo films deposited by HiPIMS 31

4.3.2 Cu films deposited by HiPIMS 36

4.3.3 Cu films deposited by DCMS 44

5 Summary and Conclusions..50

6 Literature 52

1 Introduction

The fabrication of flexible solar panels, foldable displays, different entertainment devices as well as wearable biomedical sensors has become an interesting field of research in recent years [1]. These modern technological devices contain various electronic components such as thin film transistors (TFTs), transparent conductors, metal interconnections, etc. [2]. Most of these components are based on thin metallic films, which are deposited on flexible polymer substrates and have gained considerable importance in recent years [3]. For example, although organic materials have already been successfully utilized as semi-conductive materials within TFTs, it is their insufficient durability concerning electric conductivity which made them incapable for using them as electric contacts. According to their high conductivity compared to organic materials, thin metal films are generally used as interconnections and electrodes [3]. The mentioned new electronic devices are expected to be established as consumer products in the near future, e.g. curved displays are already in commercially available. It is important that the electrical and mechanical properties are maintained over a wide range of different loading conditions such as stretching, twisting, bending and combinations of these, but unfortunately, the reliability of such devices is still an issue, e.g. for small bending radii [4,5]. Moreover, materials with different mechanical properties, from ductile to brittle, are used during the production of these devices [1]. Therefore, the deformation of each of those thin films and the evolution of cracks are of high importance and need to be investigated in detail in order to evaluate their reliability and thus enable the introduction of mass production [4]. Much effort is put into improving the properties of the thin films, but the majority of the conducted research focused on the properties and behaviour of the metallic thin films while the influence of the substrate material is often not taken into account.

In this thesis, the change of electrical and mechanical properties of metallic thin films on different polymer substrates was investigated. For this purpose, polyimide from two different producers with different thicknesses was used. The substrates were coated by applying two different physical vapour deposition (PVD) processes, namely, direct current magnetron sputtering (DCMS) and high-power impulse magnetron sputtering (HiPIMS).

After the deposition, the morphology and crystal structure were investigated with scanning electron microscopy (SEM) and X-ray diffraction analysis (XRD), respectively. Tensile testing was performed to investigate details about the electromechanical behaviour of these films during straining. Measurement of the electrical resistance during straining with and without optical analysis like confocal laser scanning microscopy were conducted to correlate the

mechanical properties of the films with the electrical ones. Further, the crack onset strain (COS) and crack density on the different substrates were determined and compared. The thermal stability and the mechanical properties of the polyimide substrates were evaluated by differential scanning calorimetry (DSC) and uniaxial tensile tests, respectively.

2 Theoretical Background

2.1 Physical Vapour Deposition

PVD processes are atomistic deposition processes that are typically used to deposit thin films within the range of a few nm to a few µm on a substrate [6]. PVD techniques can be used to coat different materials, such as metals, ceramics or polymers [7]. During the process, a material is vaporized from a solid or, less frequently, from a liquid source material in form of molecules or atoms, transported to the surface of the substrate where it condenses and nucleates as a thin film [6]. The vapour phase in PVD processes is often a plasma which contains ions, electrons and neutrals, i.e. atoms or molecules and can either perform a reaction with the background gas in the chamber or the process can be conducted in vacuum. In vacuum the mean free path between collisions with the gas atoms and/or molecules is high restricting undesired interactions [8-10]. There are several main categories of PVD, which are electron beam evaporation, sputter deposition, arc vapour deposition and pulsed laser deposition [6]. In the following, methods used within this thesis are explained in more detail.

2.1.1 Sputter Deposition

Sputter deposition is one of the most common and widely used PVD techniques. The bombardment of a surface, called target, with atomic-sized particles in order to evaporate atoms by momentum transfer is called sputtering [6]. These particles are generally ions. There are two methods to produce ions and sputter the target. One method is to use an ion source which points towards the target. The second method uses plasma. A simple way to produce a plasma is by creating a glow discharge between a cathode (target) and an anode, commonly the chamber wall, by applying a dc voltage between 500 and 5000 Volts and with the help of a process gas. This setup is called dc diode sputtering [11]. After obtaining a vacuum, the process gas, usually Ar due to its inertness, low cost and similar atomic mass to most of target materials, is introduced into the sputtering chamber [7]. In the glow discharge, the Ar atoms are ionized and accelerated by an electric field towards the target. The energy of the ions is mainly dissipated in heat as they collide with the surface. To a lesser extent the energy is transferred to the atoms near the surface, which can be ejected if the energy is higher than the binding energy [8]. The evaporated particles are mostly neutral and can escape the electric field towards the substrate, where they condense and form a film or a coating. Since the material is evaporated because of momentum transfer and not thermally, almost every solid substance can be sputtered. During the sputtering process, secondary electrons are emitted

from the surface as well, which cause further ionization of the process gas maintaining the gas discharge [11]. The ionization cross-section peaks at electron energies of about 100 eV and declines rapidly with increasing energy. In the cathode region electrons reach high energies by acceleration in the electric field. Thus, many secondary electrons in a dc diode plasma can travel through the whole apparatus and will hit the anode or are lost to the chamber walls. These high energetic electrons will cause heating of the substrate, which could limit the choice of materials to be coated. To minimize this drawback, several other sputtering techniques have been developed with magnetron sputter deposition being the most important one [7,8]. The big success of magnetron sputtering is due to a pronounced increase in deposition rate as compared to the rate achievable in dc diode sputtering [12].

2.1.2 DC Magnetron Sputtering

A magnetron uses strong magnetic fields to alter the plasma during the sputter deposition process by confining the electrons near the surface of the target. The electric field accelerates the secondary electrons perpendicular to the target surface, while the configuration of the magnetic field is engineered so that the magnetic field lines are in some parts parallel to the target. This results in an E x B drift force, where the electrons now perform are cycloidal movement and which cause an increase of their residence time near the target surface. Because of the longer residence time of the secondary electrons, ionizing collisions with the gas atoms in this region are more likely to occur. The most frequently used configuration is the planar magnetron design (Fig. 2.1). Here, the permanent magnets are placed behind the target creating a circular magnetic field [7,8]. The magnets are arranged in such a way that one pole is positioned behind the centre of the target where the second pole, consisting of a ring of magnets, is put around the edge of the target [13]. Unfortunately, the magnetic field in this setup varies over the target surface and will lead to a nonuniform plasma region and, hence to a nonuniform erosion zone on the target, which is called racetrack and possibly corresponds to nonuniform film growth on the sample. With moving magnets behind the target in a complex pattern a higher target usage and more uniform film depositions can be achieved [7,8].

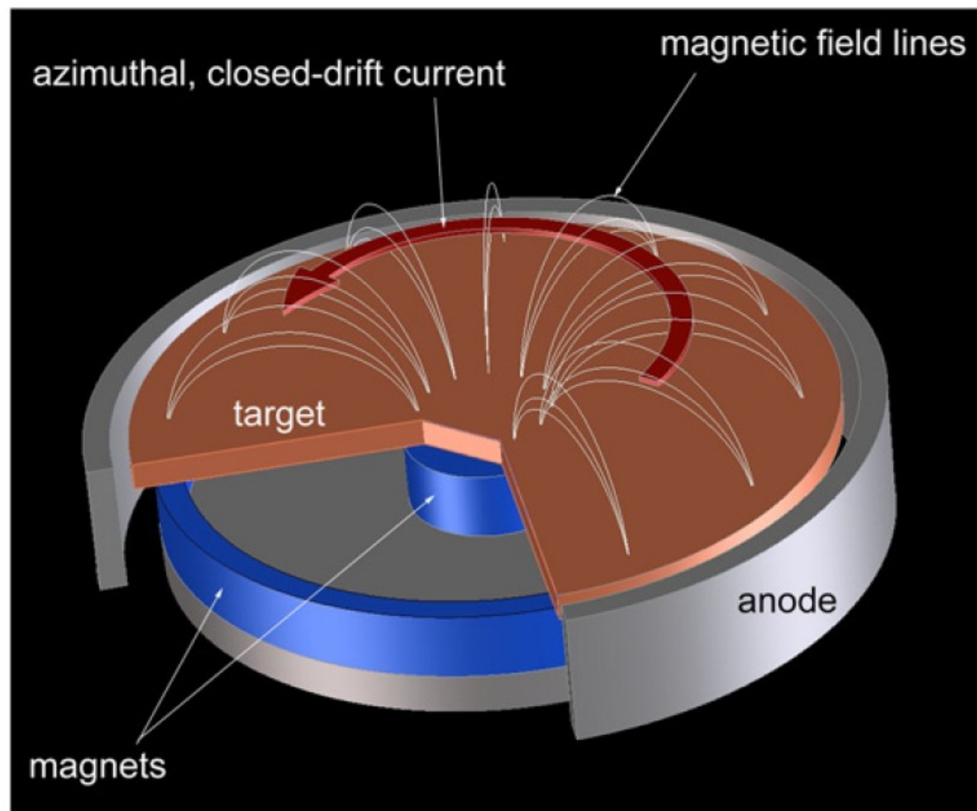

Fig. 2.1: Illustration of a planar magnetron [14].

There are two main designs of magnetrons (see Fig. 2.2) which are called balanced or conventional magnetrons (CM) and unbalanced magnetrons (UBM). In conventional magnetrons the inner and outer magnets are placed in such a way that all magnetic lines are closed between the two poles [15]. The plasma region is confined to the target and will expand several tens of mm in from the target surface. If a substrate is placed in that region, it will experience a concurrent ion bombardment, which can strongly influence the properties and the structure of the growing film. As the plasma density is low beyond this area, it cannot be used to modify the structure of the film in most cases. Furthermore, an increase in ion energy would lead to higher film stresses and subsequent film defects. Therefore, it might be very difficult to produce a dense film on large substrates using CM [13].

Compared to a balanced magnetron, an unbalanced magnetron has several lines of the magnetic field that are not closed between the inner and outer pole. If these lines are directed to the chamber walls it is called type-1 UBM. In case of type-2 UBM, the outer pole becomes much stronger than the inner one which directs the unclosed magnetic field lines toward the substrate which are typically placed opposite to the target as depicted in Fig. 2.2. High ion current densities of relatively low energy can be extracted from the plasma to form dense films without large intrinsic stresses on the substrate [13,15].

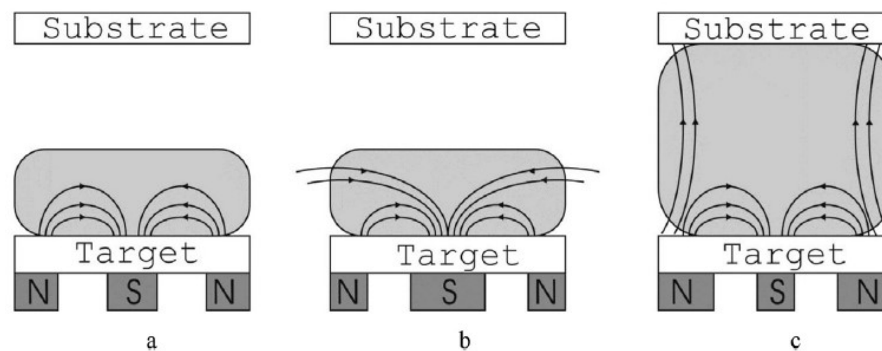

Fig. 2.2: Designs of magnetrons: a) conventional magnetron b) type-1 unbalanced magnetron c) type-2 unbalanced magnetron [15].

2.1.3 High-Power Impulse Magnetron Sputtering

The ionization of the plasma particles in a magnetron sputtering process remains very low, which causes a low total ion flux [16]**.** There is a need to use a high bias voltage to increase the energy that is provided to the deposited atoms. Furthermore, the ionization rate of the target atoms is typically below 1%. This leads to a situation, where mostly Ar ions are bombarding the substrate and can cause ion subplantations in the film leading to severe lattice defects. It was shown that operations with a common sputtering source in a pulsed mode can achieve peak target currents that are two orders of magnitude higher than the average current in in the conventional dc mode. Moreover, the pulsed mode leads to a very dense plasma with electron densities of about 10^{18} m^{-3} compared to 10^{14} – 10^{16} m^{-3} in the dc mode. Kouznetsov [17] showed that with this technique an ionization rate of the target atoms up to 70% are achievable [16].

HiPIMS power supplies produce a low average power by using high peak voltages as well as high peak energies during a low duty cycle [6]. Peak powers up to several MW/pulse with a duration of about 100 to 150 µs can be generated, which causes a low substrate temperature during the deposition [8,16]. In comparison to the dc magnetron sputtering the sputter deposition rate of this process decreases due to the pulsed voltage which is a disadvantage. A disadvantage of this process is that due to the pulsed voltage the deposition rate is decreased compared to the one in DCMS with the same energy input [6].

Simple glow discharge devices and magnetrons have the drawback that they are prone to switch to arcing. The arc is an unwanted discharge during sputtering due to high currents which produce cathode spots on the target. These spots might emit droplets and, hence,

reduce the quality of the coatings significantly. This problem increases using a pulsed mode. To suppress the formation of an arc, HiPIMS power supplies have an arc detection. Whenever an arc is detected a short interruption of the process occurs [14].

2.1.4 Sputter Yield

A key property for characterization of the sputtering process is the sputter yield *Y*, which is the ratio of the number of ejected atoms to the number of incident ions. It depends on the chemical bonding of the target atoms and the momentum transfer during the collision. In general, sputtering is less energy-efficient than thermal vaporization which causes much higher vaporization rates [6]. P. Sigmund developed theories describing the sputter yield as a function of energy in 1969 [18]. According to his work, the sputter yield of low energy ions (E < 1keV) can be calculated by

$$Y = \frac{3}{4\pi^2}\alpha\frac{4M_1M_2}{(M_1+M_2)^2}\frac{E}{U_s} \qquad (1)$$

where M_1 and M_2 are the masses of impinging ion and the surface atoms of the target. E is the energy of the ion, U_s the surface binding energy and α a dimensionless parameter depending on mass ratio and ion energy. Equation (1) shows that the sputter yield increases linearly with increasing ion energy and is inversely proportional to the binding energy of the surface atoms. The momentum transfer reaches a maximum, when $M_1=M_2$ [8]. For a given ion mass and target, the sputter yield can be calculated as a function of energy to obtain the maximum as well as the minimum threshold energy that is characteristic for the used ion-target combination. Ion energies below 50 eV cause sputter yields in the range of 10^{-2}-10^{-6} because the ions can only eject the weakest bound atoms. Energies in the range of 100 eV to 1 keV are of most importance as the sputter yield increases rapidly. In this regime, *Y* is in the range from 0.1 to 3 for most materials of technological interest. The key feature of this region is an almost linear dependence of the ion energy and the sputter yield (see Fig. 2.3). Above an energy of about 1 keV collision cascade-like behaviour is witnessed, where one ion has enough energy to eject multiple target atoms. For industrial purposes, this regime is less useful, because of the high energies needed and the high energy of the ejected atoms. Ion energies above 50 keV lead to ion implantation into the target and a decreased sputter yield [7].

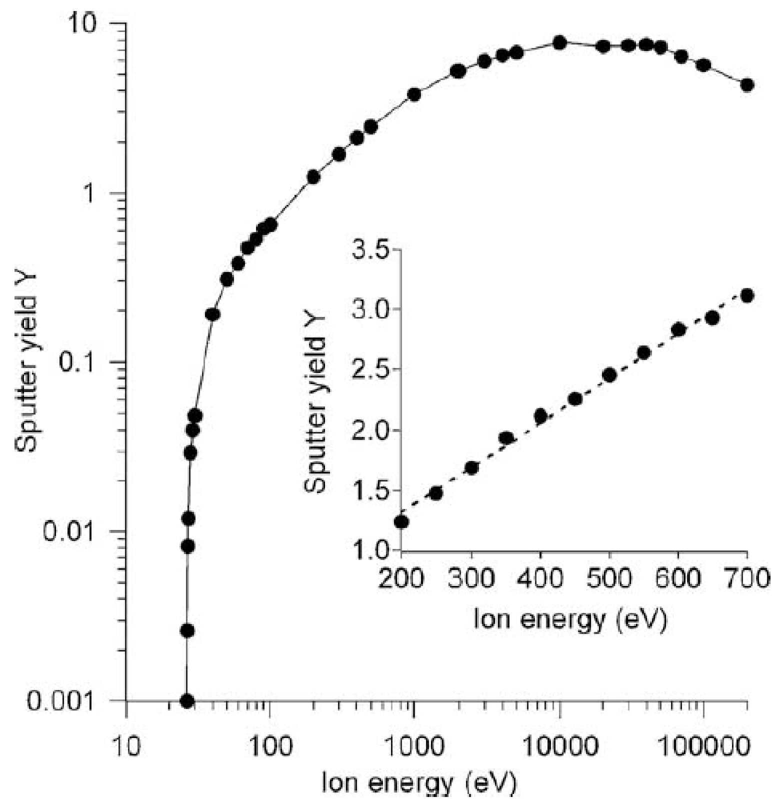

Fig. 2.3: Sputtering yield *Y* of Cu as a function of the energy of Ar ions [8].

2.1.5 Structure Zone Models

Thin film microstructures and morphologies can be displayed in a systematic way and grouped as a function of the deposition parameters, such as deposition temperature and bias voltage or technological and physical parameters like migration of grain boundaries or impurity level in structure zone models (SZM's) [19, 20].

The first SZM was introduced by Movchan and Demchishin [21] to classify the top surfaces and cross-section morphologies of very thick thermally evaporated single-phase metal films like Ti, Ni and W as well as oxide films ZrO_2 and Al_2O_3. Here, three zones were introduced shown in Fig. 2.4. Their categorization is based on the relation of the microstructure of the deposited films and the homologous temperature T_S/T_m, where T_S is the substrate temperature and T_m is the melting temperature of the deposited element. In Zone 1 ($T_S/T_m <$ 0.3) the surface diffusion is limited and a formation of tapered crystals with domed tops is predominant, which are separated with voided boundaries. In Zone 2 ($0.3 < T_S/T_m < 0.5$) the surface diffusion is increasing which results in closed voids and a tightly packed columnar texture. The grain sizes increase with T_S/T_m and may increase through the whole film thickness.

The mechanical properties of the deposited metal are similar to cast metal and the surface has a mat appearance. Zone 3 ($0.5 < T_S/T_m < 1$) is characterized by equiaxed large grains as a result of surface and self-diffusion. The size of the grains grows with increasing T_S/T_m value. The properties in this zone are similar to an annealed metal [22].

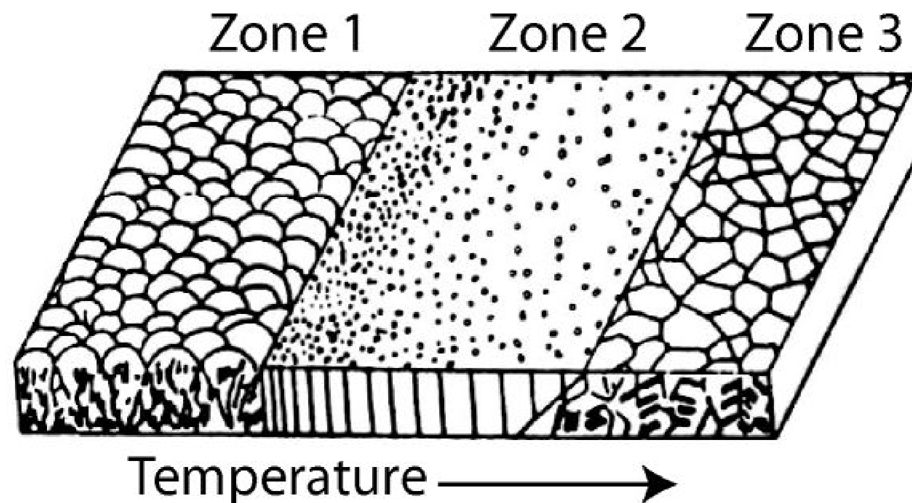

Fig. 2.4: Structure zone model of Movchan and Demchishin for qualitative classification of thin-film morphology [23].

Thornton extended the SZM by Movchan and Demchishin and added an additional axis, which accounted for the influence of the sputtering gas (Ar). He proposed another diagram shown in Fig. 2.5. Here, in Thornton's model another zone, the so-called transition zone between Zone 1 and Zone 2, or Zone T, was added. The morphology of Zone T is characterized by densely packed fibrous grains that do not extend through the whole thickness of the film and is dependent on the working gas pressure. If the pressure increases, the mean free path of the particles decreases as they undergo elastic collisions with the working gas leading to a smaller kinetic energy. Therefore, the adatom mobility is reduced and shows a Zone 1 morphology [22-24].

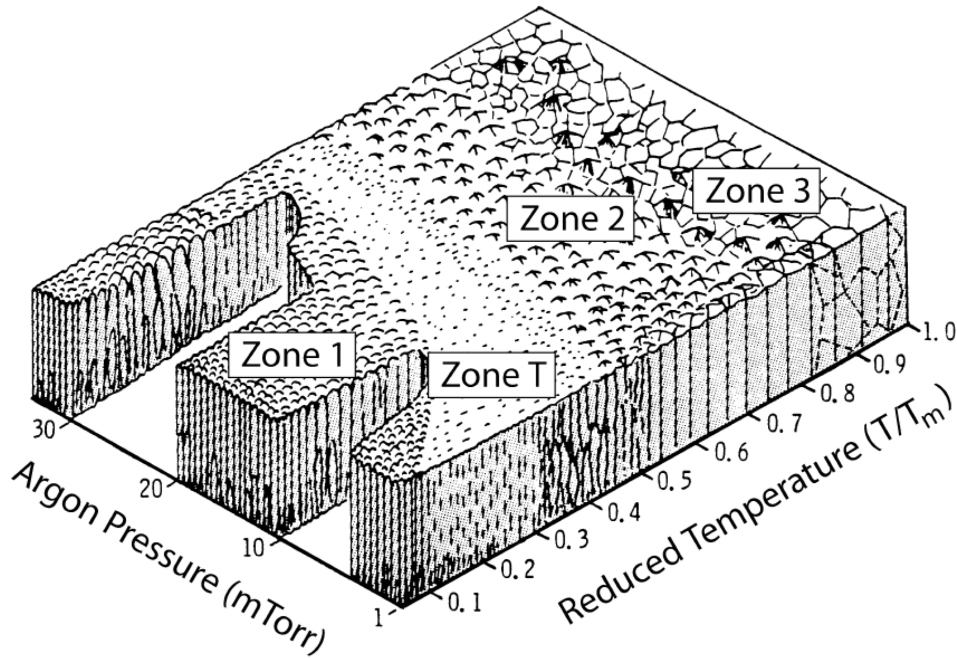

Fig. 2.5: SZM proposed by Thornton for classification of morphologies realized by PVD [22].

2.2 X-ray Diffraction

One of the most common techniques to analyse crystallographic structures is XRD. In order to gain information about the crystal a sample gets penetrated with X-rays. While a large part of the X-rays penetrate the examined material unhindered, some get diffracted at certain points of the crystal lattice (see Fig. 2.6). To get a detectable reflection the Bragg condition must be fulfilled [25, 26]:

$$n\lambda = 2d \sin \theta_B \tag{2}$$

Bragg's law states that different diffracted waves show constructive interference, if a multitude of *n* (*n*= 1,2,3…) multiplied with the wavelength λ of the incident beam is equal to two times the lattice parameter *d* multiplied with the sine of the Bragg angle θ_B**.** If the Bragg condition is not fulfilled, the waves interfere destructively and no diffraction reflex occurs [27].

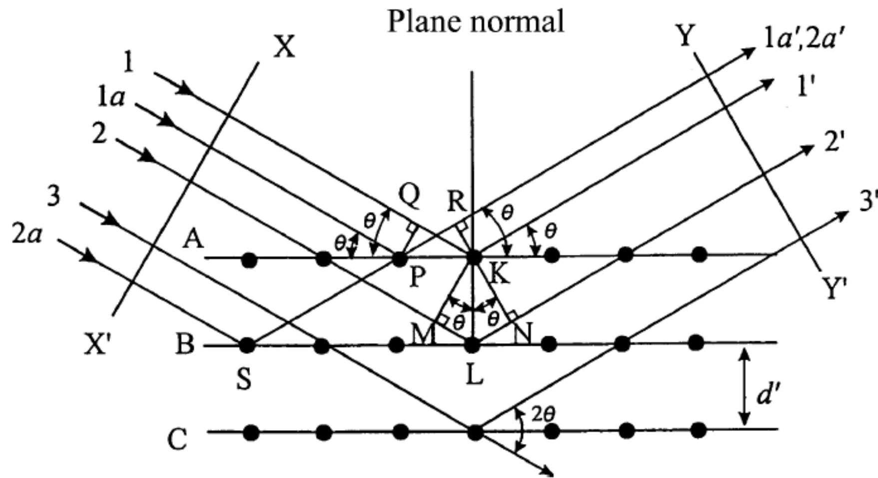

Fig. 2.6: Schematic representation of X-ray diffraction on a crystal [25].

X-rays are produced in an X-ray tube which consists of two electrodes where one is used as source of electrons. In the tube, the electrons are accelerated in an electric field between the electrodes towards to the anode, where they collide with the surface and decelerate in a short time. During this process continuous Bremsstrahlung with various wavelengths is emitted. If the electrons have enough energy to eject an inner shell atom of the anode material, the atom will become excited. To regain its stable state, an outer shell electron will jump to the inner one. The abundant energy will be released as a radiation photon, whereby its energy is characteristic for the target material [25, 28]. The target materials frequently used are Cu and Mo, but also Cr, Ga, Fe and W can be utilized [27,28]. In Fig. 2.7 a schematic example of an X-ray emission spectrum is pictured.

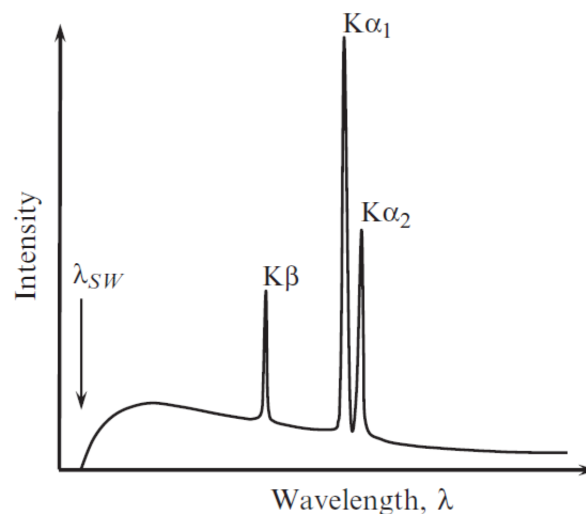

Fig. 2.7: Schematic representation of a typical X-ray emission spectrum, with the presence of a continuous background and three characteristic wavelengths: $K_{\alpha1}$, $K_{\alpha2}$, and K_{β} [28].

$K_{\alpha 1}$ and $K_{\alpha 2}$ are the peaks connected to the occasion when an electron performs a transition from the L shell to the K shell, K_{β} when an electron is transferred from the M shell to the K shell [25,28].

After diffraction, the beam is recorded by a detector measuring the intensity of the beam. X-rays can produce different effects with matter e.g., electric current, generate particles etc., which can be registered and are used to gain information. Detectors can be classified on the capability of resolving the location where the photon has been absorbed. Basically, there are point (0D), linear (1D) or area (2D) detectors. Point detectors can only measure one intensity at a time and must be moved over an 2θ angle range to record the diffractogram. Spatial resolution is supported by a linear detector, whereas resolution in two dimensions is covered by area detectors. Fig. 2.8 shows a typical result of a diffractogram and the capabilities of the detectors [28].

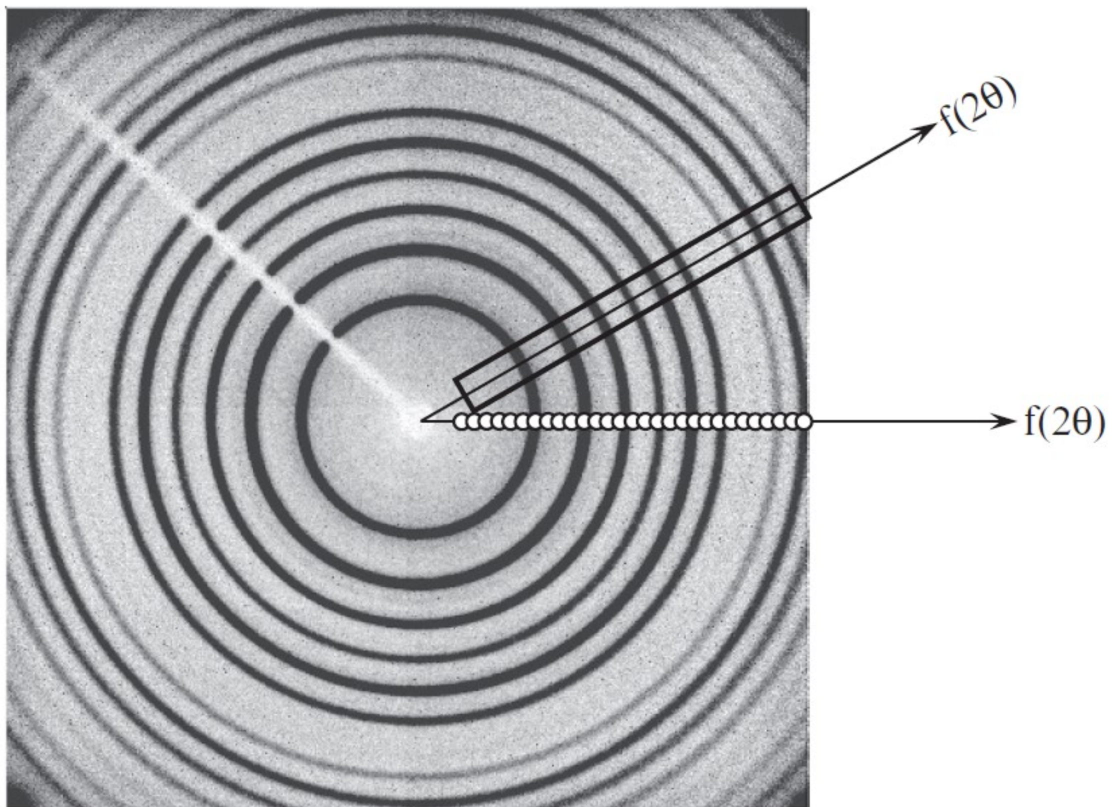

Fig. 2.8: Schematic representation of point (discrete dots), line (solid rectangle), and area (entire picture) detectors [28].

2.3 Differential Scanning Calorimetry

DSC is a measurement technique to obtain the heat flow rate or heat flux ϕ, or rather the change of the difference of the heat flow rate of a sample and a reference sample. This allows the measurement of different thermal properties like transition temperatures, melting point, recrystallization point, glass transition temperature as well as heat capacity due to detectable endothermic or exothermic reactions. There are two main designs in use namely the heat flux DSC and the power compensation DSC. For this thesis only the heat flux DSC design was used [29].

In heat flux DSCs, an exchange of heat with the surrounding area can be obtained by knowing the heat conduction path and the given thermal conductivity. The main measurement property is the temperature difference ΔT between the sample T_S and a reference sample or the furnace T_F, which defines the intensity of the exchange [29, 30]. The heat flow rate is proportional to ΔT and defined as

$$\phi = -\frac{A}{\Delta x}\lambda(T)(T_S - T_F) \tag{3}$$

where A is the cross-sectional area, $\lambda(T)$ is the temperature dependent thermal conductivity, Δx is the length of the conduction path, T_S is the temperature of the sample and T_F is the temperature of the furnace [30].

There are different ways to realize the heat exchange path, where the disk-type is the most commonly used (see Fig. 2.9). Thereby the main heat flow from the furnace passes through a medium conductive disk, which consists of a metal, ceramic or quartz glass. Temperature sensors are placed in the disk around the centre where the samples or crucibles are placed on. Thus, there is no dependence on the placement of the sample in the crucible [29]. The crucibles need to have a large heat capacity and thermal resistivity compared to the sample to decrease their influence on the measurement. The heating of the furnace is most commonly linear:

$$T_F = T_0 + \beta t \tag{4}$$

Here, β represents the heating rate, t the time and T_0 the starting temperature of the furnace. It should be noted that only if a reaction or transition takes place ΔT varies from zero [30].

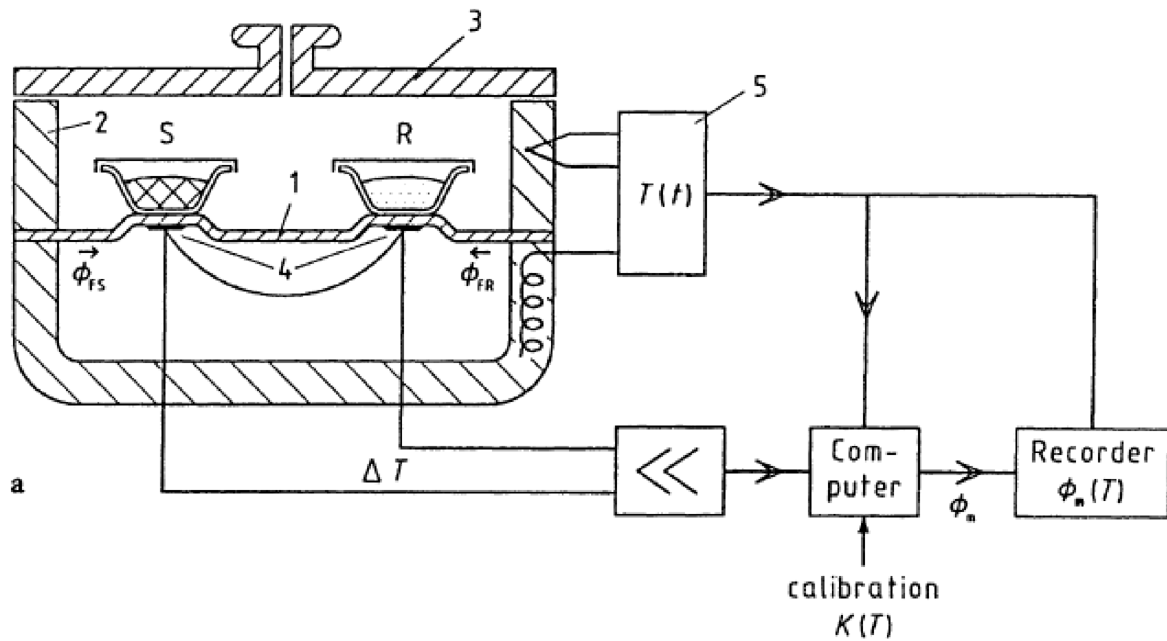

Fig. 2.9: Representation of a heat flux DSC with disk-type measuring system. 1 - disk, 2 - furnace, 3 - lid, 4 - differential thermocouple(s), 5 - programmer and controller, *S* - crucible with sample substance, *R* - crucible with reference sample substance, ϕ_{FS} - heat flow rate from furnace to sample crucible, ϕ_{FR} - heat flow rate from furnace to reference sample crucible, ϕ_m - measured heat flow rate and *K* - calibration factor [29].

2.4 In-situ 4-Point Probe Measurement

The 4-point probe measurement is a common technique to obtain electric phenomena of a specimen. When an electric resistance measurement is performed by attaching only two wires to the sample, the contact resistance in addition to the resistance of the wires can be determined. For measuring small resistances this can lead to very high deviations from the correct values. This effect can be eliminated by using 4-point probe measurements. The basic principle of the electrical 4-point probe resistance measurement is presented in Fig. 2.10. Here, the current I runs through the two outer contacts and the changing voltage U_m is measured between the inner contacts. A small current runs through the voltmeter and causes a decrease in voltage as the resistance in the voltmeter is not infinite. The change of voltage although is very small compared to 2-point probe resistance measurements and therefore also the measurement error. With the help of Ohm's law,

$$U_m = R_x I \tag{5}$$

the resistance R_x can be calculated [31].

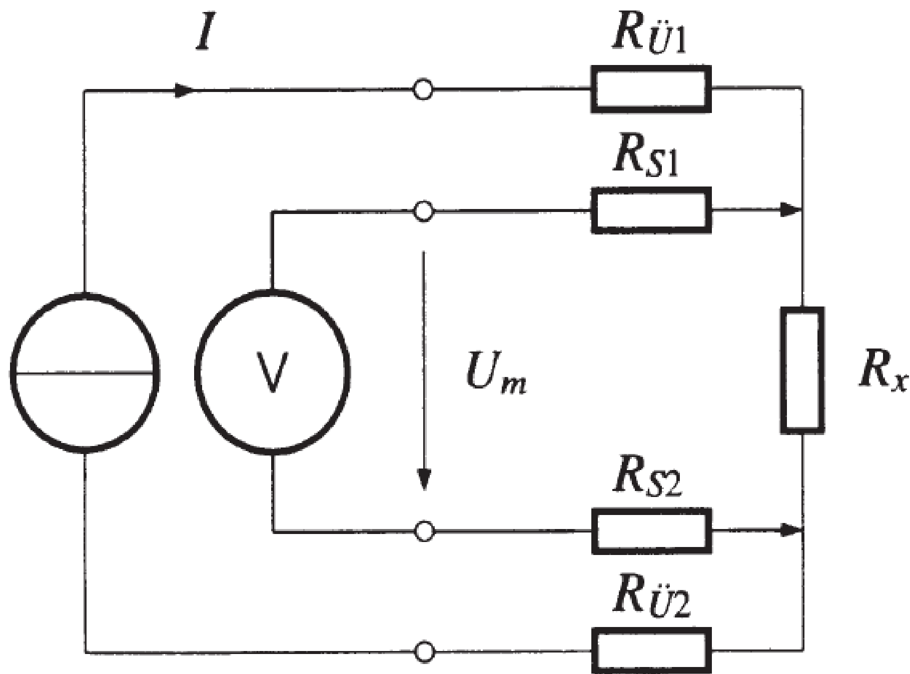

Fig. 2.10: Schematic presentation of the 4-point probe measurement technique. I represents the current, U_m the voltage, R_x the resistance of the sample, $R_{Ü1}$ and $R_{Ü2}$ the resistance of the electric wires as well as R_{S1} and R_{S2} the resistance of the potential clamps [31].

Using this technique in-situ while performing mechanical loading, the change in resistance has two main causes. First, there is a geometrical change of the sample. Under mechanical load the sample witnesses an elongation of the distance between the contacts while decreasing its cross-sectional area. Second, structural changes like necks, cracks, delamination and so on can occur and result in resistance changes. For the first case, if only the geometry changes and no defects occur, the resistance before straining is defined by

$$R_0 = \frac{L_0 \rho}{A_0} \tag{6}$$

where L_0 is the initial distance between the contacts, ρ is the resistivity and A_0 is the initial cross section. During straining the resistance is given by

$$R = \frac{L\rho}{A} \tag{7}$$

where $L=L_0+\Delta L$ is the instantaneous gauge length, the strain is defined by $\varepsilon=\Delta L/L_0$ and A is the instantaneous cross section. It is assumed, that during plastic deformation of the conductive thin film, the volume and resistivity stays constant and the resistance is defined by

$$\frac{R}{R_0} = \left(\frac{L}{L_0}\right)^2 = (1+\varepsilon)^2 \quad (8)$$

When a thin film faces structural modification such as cracks, equation (8) is not applicable anymore (Fig. 2.11). At the point where the two lines deviate, the COS can be determined [2,4,5].

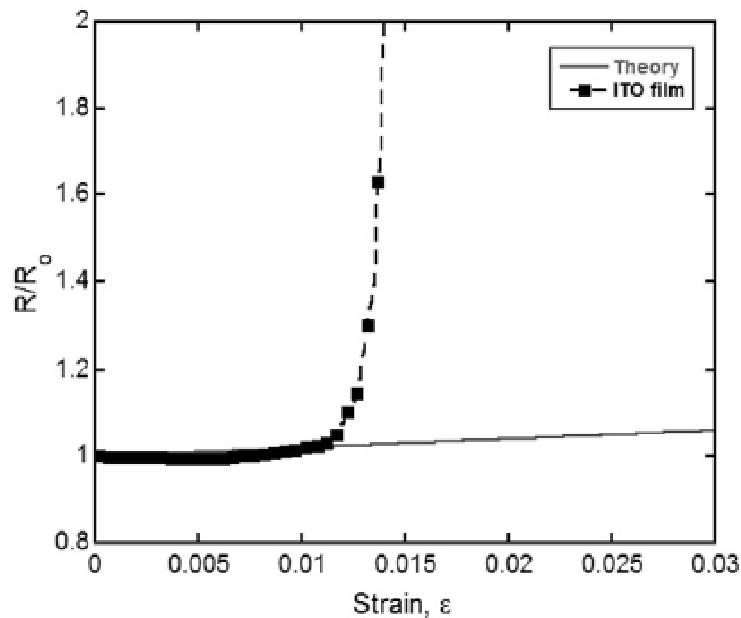

Fig 2.11: Normalized electrical resistance of an indium-tin oxide film as function of strain compared to the theory line [4].

2.5 Optical in-situ measurements

Thin films can be strained while optical devices are used to observe the nucleation and growth of cracks and necks, delamination, evolution of bucklings, etc. For brittle thin films optical microscopes or SEMs can be used. Brittle films fracture by forming through-thickness cracks perpendicular to the straining direction (see Fig. 2.12b). Ductile films, however, deform at low strains by forming necks and at high strains through thickness cracks (see Fig. 2.12). Due to small topographical changes of the surface in ductile thin films during straining**,** atomic force microscopy is a useful tool for investigation [4].

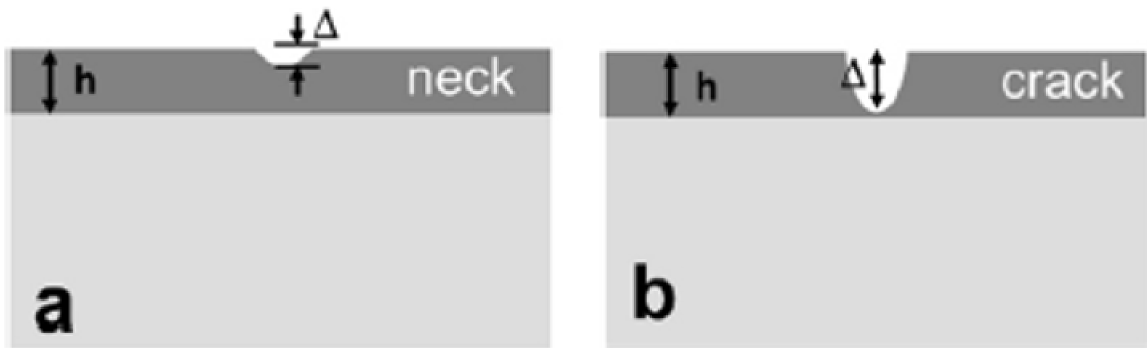

Fig 2.12: Schematic representation of a) a neck and b) a through-thickness crack [4].

During the in-situ measurement, the strain, when first cracks occur, is called COS. This COS can be used to determine the interfacial fracture shear stress. The crack spacing at saturation λ can be determined by optical devices. This property is explained by the shear lag model. Here, two cracks in the distance L have been formed in the thin film (see Fig. 2.13 (i)). After the sample is strained, a reasonable approximation for the shear stress τ in the coating-substrate interface can be obtained as seen in Fig. 2.13 (ii). The tensile strength in the coating fragment is seen in Fig. 2.13 (iv). Now new cracks can form anywhere in the area of CC' because the tensile stress σ is bigger than the fracture stress σ'. Each new crack will change the stress distribution. So, the nucleation of cracks will continue as long as the space between adjacent cracks has still a region where $\sigma \geq \sigma'$. After that, a saturation phase is reached where no new cracks occur even with higher strain. Now, the shear stress at the interface is limited to the plastic shear stress of the ductile substrate. Experiments show that the crack spacing at saturation should range between a minimum and a maximum. The nearest new crack can occur at position C (Fig. 2.13 (v)). The largest spacing between the cracks can be λ'. The minimum and the maximum crack spacing have a difference by a factor 2 [32, 33].

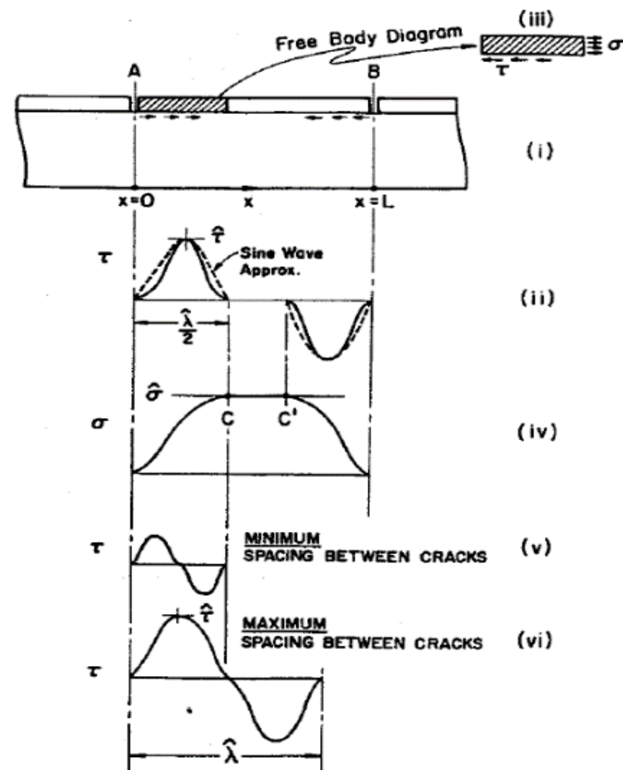

Fig. 2.13: Stress distribution at an interface and through the thickness of the film when transverse cracks are formed [32].

2.6 Polyimides

The oldest and best-known high-performance polymers are polyimides. In 1953 DuPont first patented the new polymer in the United States. Later in 1963 highly heat-resistant lacquers and foils based on this polymer reached the market. Today, different brands and producers are well-known for their polyimide products such as [34]:

- Polyetherimid PEI: Ultem (GEP)
- Polybismaleinimid PBMI: Kerimid, Matrimid, Rhodeftal (Huntsman)
- Polyamidimid PAI: Torlon (DSM)
- PI-foil: Kapton (DuPont)
- PI-semi-finished parts: Vespel (DuPont)
- TPI „Aurum“ (Mitsui)
- PI-foil: Upilex (UBE Industries)

The heat resistance of polyimides is very high, especially for aromatic polyimides. These contain the characteristic imide group (see Fig. 2.14) [34]. Rigidity and strength of polyimides are very high which is due the fact that the aromatic ring connections, that are built in linear, thread arranged macromolecules, are forced together [35]. Unfortunately, they show a low notch impact strength but good wear behaviour. Dependent on their formation, they are either classified as duroplastics/thermosets or thermoplastics [34].

The maximum usage temperature for unfilled thermoplastic polyimides, for polyesterimides and polyetherimides, are measured to be little over 200 °C. Classical polyimides can be deployed up to 400 °C or even higher for a short period of time. Continuous operating temperatures for thermoplastic polyimides are between 170 to 190 °C and for duroplastic polyimides between 260 to 315 °C depending on the atmosphere. However, above 800 °C the polyimides are reaching their temperature limit since carbonization processes will start to occur. Although some polyimide types are referred as thermoplastics, this does not mean they can be formed in the melted state or can be re-melted after formation, as the melting temperature lays above the decomposition temperature [34,35].

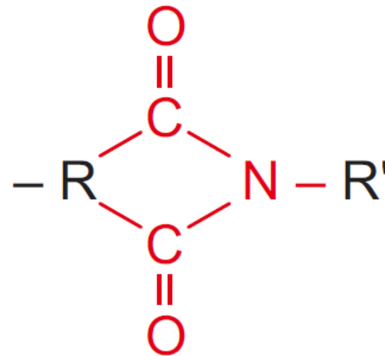

Fig. 2.14: Basic imide group used in polyimides [34].

3 Experimental Details

3.1 Film Deposition

In the present work, the deposition of the films was carried out by nonreactive, unbalanced magnetron sputter deposition using the lab-scale deposition device “Esmeralda” (see Fig. 3.1). It consisted of a cylindrical stainless- steel chamber (Ø 50 cm x 60 cm), a pumping system, control units and power supplies.

Fig. 3.1: Photograph of deposition system “Esmeralda” used in this work.

The chamber can be equipped with different sources, depending on the required deposition method. For DCMS and HiPIMS an unbalanced TORUS® Mag Keeper™ magnetron sputtering source (Kurt J. Lesker Company, USA) was used. Different sputter targets composed of either high purity Mo or high purity Cu with target sizes of Ø 76 mm x 6 mm were purchased from Kurt J. Lesker and mounted. The power supplies for the sputter source consisted of a DC power

supply model GS 30/1000 manufactured by ADL GmbH, Germany, while the pulse power generator SPIK3000A-10 was produced by MELEC GmbH, Germany. The pulse power generator can be operated in DC or HiPIMS mode, using the control software on a connected laptop.

The pumping system was realized by two consecutive pumps. First, a rotary vane pump (Pfeiffer Vacuum Duo 20) pre-evacuated the chamber to a pressure level of about 1 Pa. Subsequently, a turbomolecular pump (Pfeiffer Vacuum HiPace® 700) was connected to evacuate the chamber to a high vacuum level of about 10^{-5} Pa. The gas flow rate of the working gas Ar was adjusted by a thermal mass flow controller (Brooks Instrument, USA). The deposition system was vented first by introducing N_2 before opening the valve to the atmosphere.

A thermo-couple of the type K was attached to the sample holder near the substrate to determine the temperature during deposition.

Mo and Cu thin films with a thickness of 300 nm were deposited by HiPIMS on polyimide of different thickness (50 µm and 125 µm) and manufactured by different companies (Kapton, DuPont and Upilex, UBE Industries). In addition, a Cu film with comparable thickness (500 nm) was deposited using DCMS on all mentioned polyimides for comparison. Particular attention was paid to the substrate temperature during the deposition process to avoid carbonization or other thermally induced changes of the used polyimide.

Prior to the deposition, the polyimide substrates and additional (100) Si substrates, for obtaining the film thicknesses, were ultrasonically cleaned in an ethanol bath for 10 min and afterwards air dried. After cleaning, the substrates were fixed on a substrate holder with Kapton tape. The configuration can be seen in Fig 3.2. The sample holder was placed in the steel chamber at a distance of 14 cm to the magnetron when using HiPIMS and at 8 cm when using DC deposition mode (Fig. 3.3).

For HiPIMS the deposition power was set to an average of 400 W with a pulse length of 200 µs and a pulse repetition frequency of 100 Hz. The waveforms of the voltage and current were recorded by an oscilloscope (Tektronix TPS2024) and an example for Cu deposition is presented in Fig 3.4. Here, the discharge voltage is about −560 V during the pulse, while the target current reaches a peak of about 45 A. The deposition time was set to 30 min for Mo and 8 min for Cu to produce films with comparable thicknesses.

After the electro-mechanical tests, the Cu thin film was reconsidered and evaluated. Another approach was made to change the properties of the Cu film and gain ductility. Therefore, the DCMS deposition mode was used with the same average deposition power of 400 W. The deposition time was set to 3 min to gain a film with comparable thickness. The main deposition parameters during the whole deposition process by HiPIMS for both metals used as well as the final deposition parameters of DCMS for Cu are presented in Table 3.1.

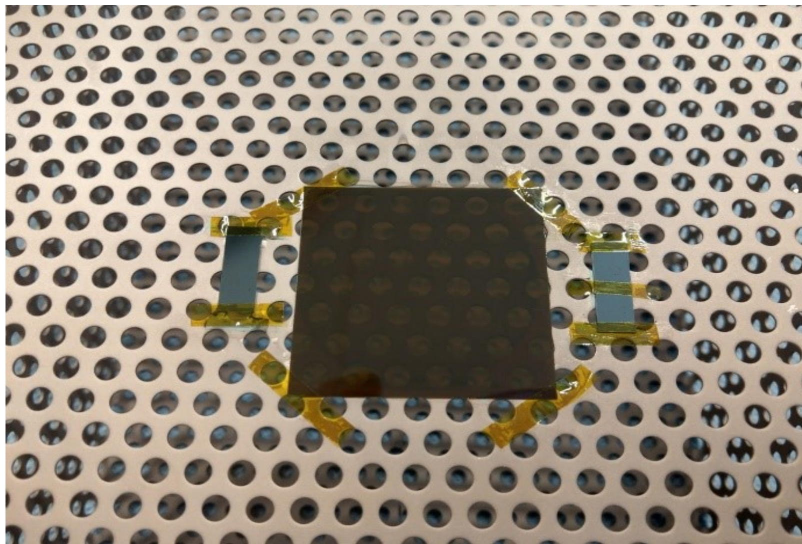

Fig. 3.2: Configuration of the polymer substrate and (100) Si substrates on the substrate holder.

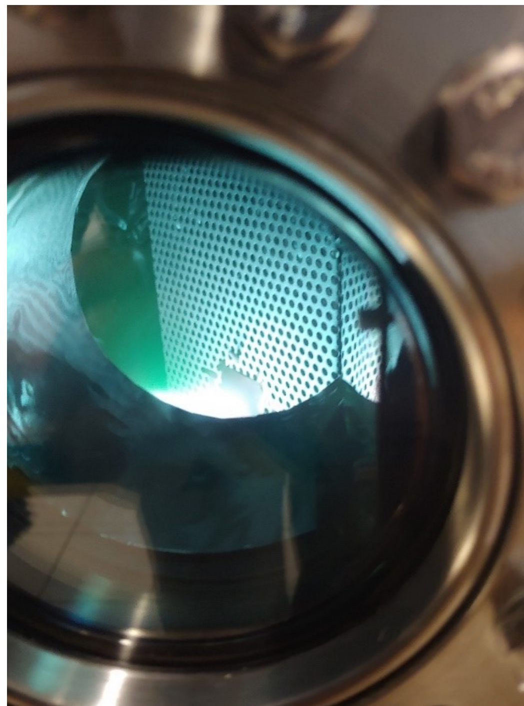

Fig. 3.3: Example of deposition process using a Cu target in HiPIMS mode.

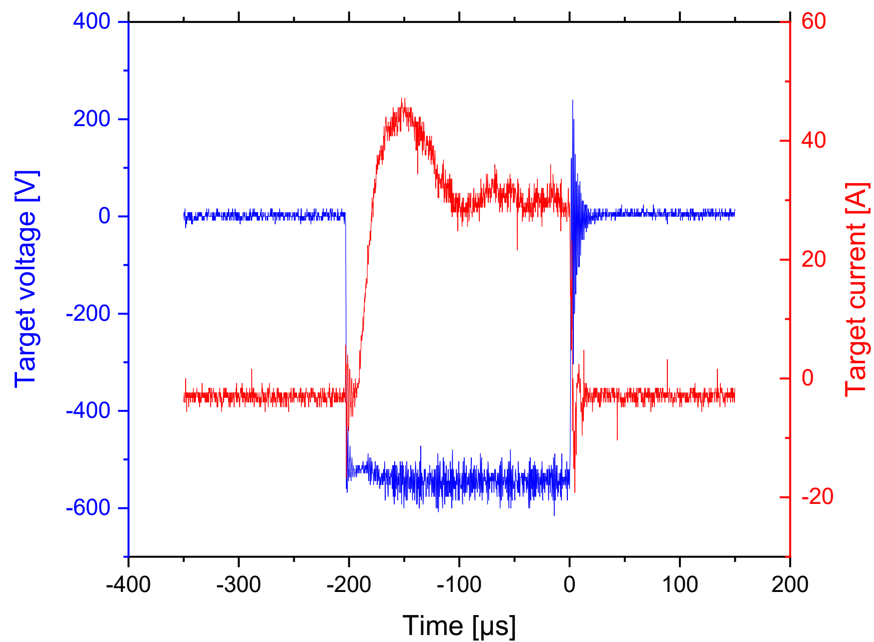

Fig. 3.4: Example for voltage and current waveforms recorded during the HiPIMS deposition process (here Cu).

Table 3.1: Main operating parameters for the film deposition of Mo and Cu.

Film	Deposition method	Time [min]	U (average) [V]	I (average) [A]	P (average) [W]	Distance to sample holder [cm]	Pressure [Pa]
Mo	HiPIMS	30	−630	0.5	400	14	1
Cu	HiPIMS	8	−560	0.6	400	14	1
Cu	DC	3	−410	0.8	400	8	0.6

3.2 Substrate Characterization

The substrate was first analysed by DSC using a Mettler Toledo Differential Scanning Calorimeter DSC 3. Any differences in the thermal properties or thermal stability should be detected and revealed with this method.

Further, a tensile test was carried out on substrate samples with modified geometry based on the DIN EN ISO-527 standard. The geometry was adapted to the existing sample material in order to continue to meet the standard. For tensile testing, a ZWICK/ROELL Z100 equipped with 200 N load cell type ZWICK/ROELL Xforce P with a sensitivity of 2 mV/V combined with flat grips ZWICK/ROELL Type 8033 was used. The data was analysed and evaluated using a Python script that was provided by the Anaconda software package. The tensile testing was modified in such a way, that 4 loading cycles were performed in the linear-elastic area to avoid or minimize alignment influences and obtain the Young's modulus of the substrates. During the fifth loading cycle, the specimen was strained until failure.

3.3 Film Characterization

The film thickness was determined by using a Wyko NT1000 profilometer. The profilometer uses white-light interferometry to obtain a high-resolution 3D image of the sample surface. The lens of the profilometer can be moved in height by a defined path length during the measurement. Light reflected from the measuring surface interferes with that of a reference's surface, which means that height information can be assigned to points on the sample.

The crystalline structure of the films was investigated by XRD using a Bruker AXS D8 Advance diffractometer. The diffractometer setup consisted of a Cu X-ray tube, a Göbel mirror and a Sol-X energy dispersive detector. The measurements were performed in Bragg-Brentano scan-geometry and in detector scan mode, where the incident angle of the X-ray beam was set to 2° in order to minimize the influence of the substrate. Used parameters are listed in Table 3.2.

Table 3.2: Operating parameters for the XRD measurements.

Tube current [mA]	Voltage [kV]	Angular range [°]	Increment size [°]	Scan speed [s per step]
40	40	20-80	0.02	1.2

Uni-axial tensile straining tests were performed on an MTS Tytron 250® universal testing machine which can record time, load and displacement. The test samples were cut from the coated substrate with a sharp knife and had approximate dimensions of 5 mm x 40 mm. The tests were performed with a constant straining rate of 5 µm/s for loading and unloading and each sample was subjected to a maximum strain of 10%. After loading, the samples were unloaded to a strain of 0% again. To correlate mechanical and electrical properties, in-situ 4-point probe resistance measurements were used. Here, the probe contacts were embedded in the grips of the straining instrument, with an initial gauge length of 20 mm. The electrical resistance was measured by a digital multimeter (Keithley Model 2000 Multimeter) and the data was recorded using a LabView script. Fig 3.5 is showing the electromechanical test setup.

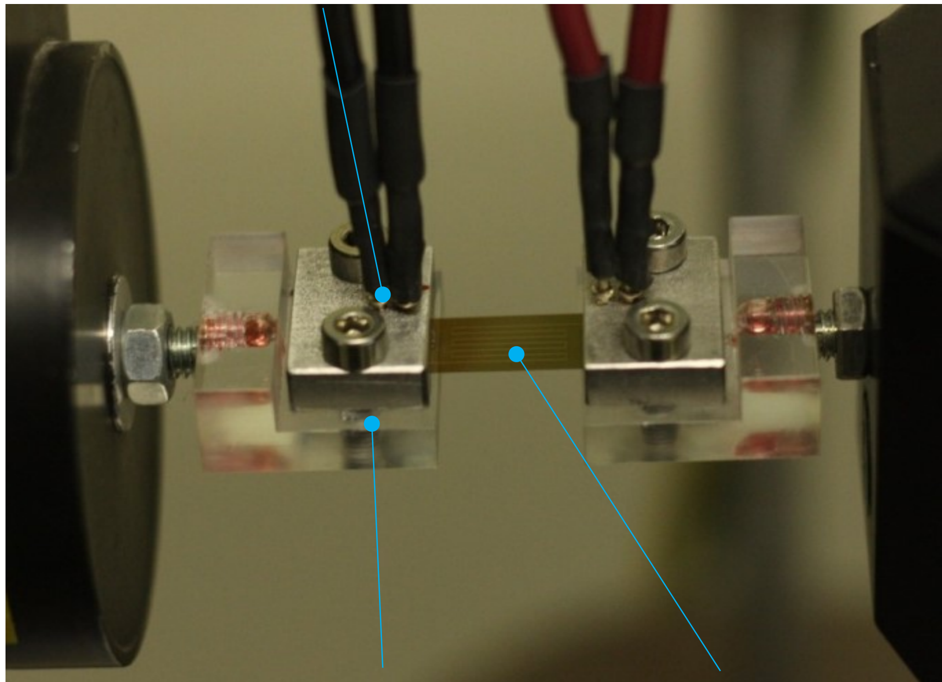

Fig. 3.5: Electro-mechanical test setup to determine the electrical resistance of the thin films during tensile testing.

Further, another in situ experiment was performed using a small-scale tensile straining device (Anton Paar TS 600) in combination with an Olympus LEXT 4100 OLS CLSM (Fig 3.6). It should be noted than only the 50 µm substrates (Upilex and Kapton) were tested with this setup. For the confocal laser microscope, long distance lenses were used for the experiments. The

samples mounted on the Anton Paar TS 600 straining device were discontinuously strained to a maximum of 16% with a displacement rate of 5 µm/s. Several pauses with a holding time of 2 minutes each were conducted to record pictures with the confocal laser microscope. The COS can be obtained while using in-situ optical measurements as well as the crack density. The crack density of each sample was investigated by using three-line profiles parallel to the straining direction and determining the average of the results using the free software Gwyddion. During straining the samples, an in-situ four-point probe resistance measurement was carried out. The connections for the resistance measurement are also incorporated in the grips of the straining device.

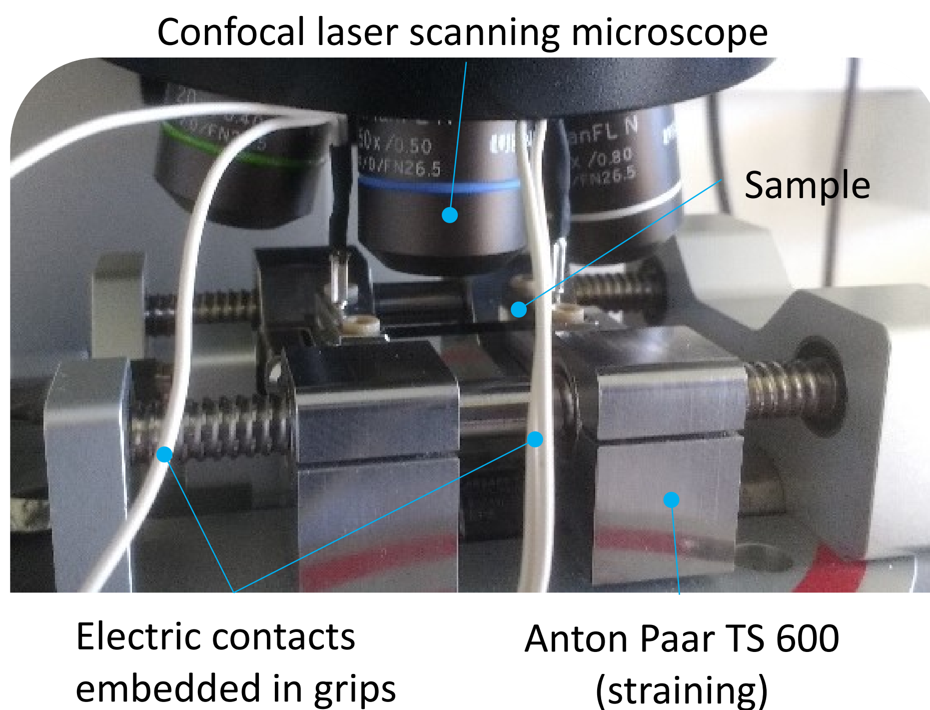

Fig. 3.6: Electro-mechanical test setup with optical device to determine the electrical resistance of the films and record 3D images of the surface during tensile testing.

4 Results and Discussion

4.1 Properties of Polyimide Substrates

In order to characterize the polyimide substrates (DuPont Kapton, UBE Industries Upilex), their thermal stability was investigated by DSC. Since the heating of the polyimide substrates, as they are exposed to plasma during the deposition process, might cause an alteration of their properties, this may also influence the investigated thin film properties. While using HiPIMS as a deposition method, a maximum temperature of 110 °C was measured with a thermocouple placed next to the substrate, whereas the maximum temperature increased to 180 °C if the deposition was made by DCMS. Fig. 4.1 shows the heat flux which is determined during the DSC measurement of Kapton. It reveals a phase change reaction at about 80 °C (red circle). Considering the maximum temperature during deposition, this indicates that the Kapton polyimide has already transitioned while being coated. In contrast the glass transition temperature is determined to be between 330 °C and 350 °C (blue circle), which means this is without influence on the film properties studied within this work.

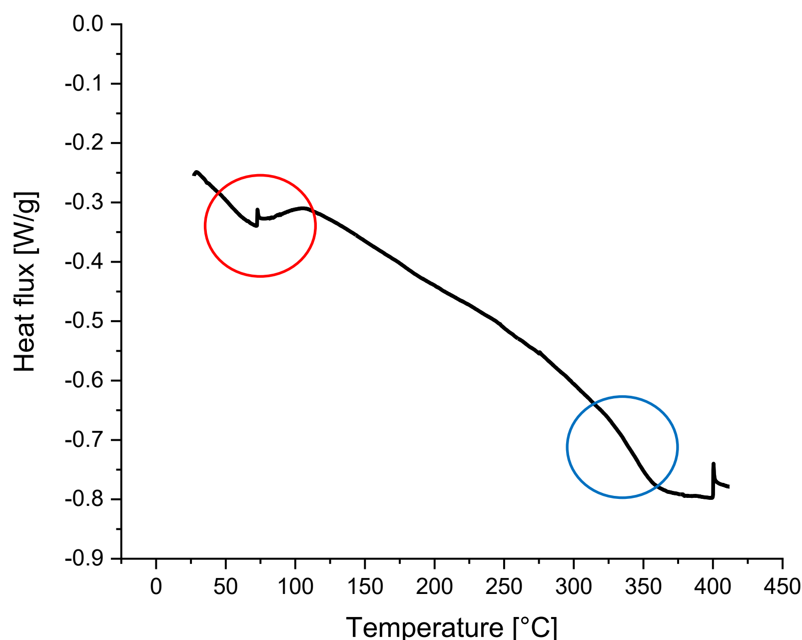

Fig. 4.1: Heat flux as a function of temperature during the DSC measurement of Kapton polyimide.

Similarly, the glass transition temperature of the Upilex polyimide is obtained to be in the range from 360 °C to 370 °C (blue circle in Fig, 4.2) and, hence, also without effect on the thin film properties. This polyimide, however, is found to be thermally stable within the measured temperature range throughout the deposition process.

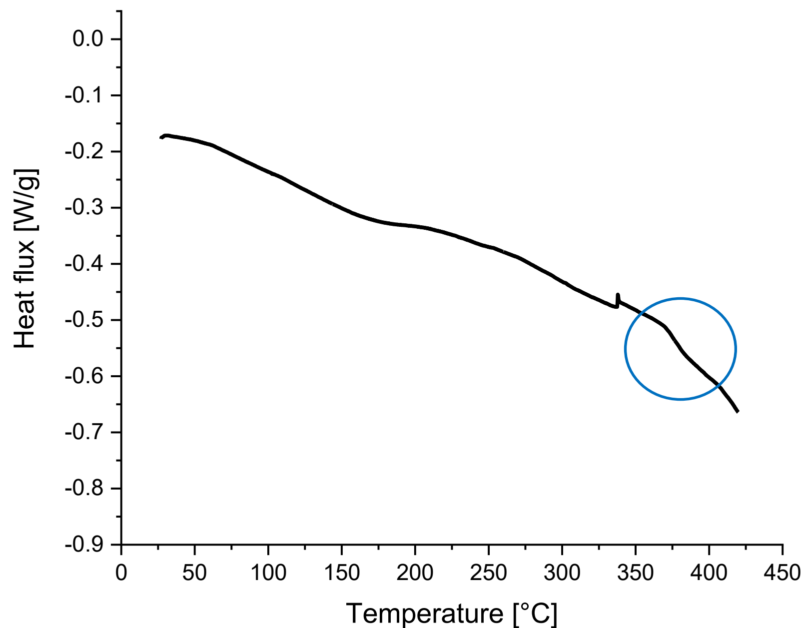

Fig. 4.2: Heat flux as a function of temperature during the DSC measurement of Upilex polyimide.

The results obtained during tensile testing are presented in Tab. 4.1 for 50 µm Kapton and Upilex polyimide as well as the manufacturer's specifications for both 50 µm substrates. Additionally, the manufacturer's information for Upilex with 125 µm is shown, as its mechanical properties differ from the ones with 50 µm thickness. This is not the case for Kapton polyimides. However, it can be noticed that the measured values for the Kapton polyimide are in good agreement with the ones provided by the manufacturer. The obtained values for the Upilex substrate are, however, below the reference values. Possible explanations for this deviation in values could be the storage conditions like temperature differences or humid air conditions and the cutting of the polyimide to the sample size needed for the tensile tests. However, it is evident that the polyimides from different manufacturers show different behaviour under mechanical stress. While the tensile strength of both polyimides is similar, the values for the ultimate straining and the Young's modulus differ significantly. Kapton tends to deform more plastically with an ultimate straining at 68%,

compared to 29% for Upilex polyimide. The Young's modulus for Upilex polyimide with a value of 8700 MPa indicates a more rigid behaviour as it is more than twice as high as the Young's Modulus for Kapton polyimide with 3700 MPa.

Tab 4.1: Mechanical properties of polyimide substrates obtained from tensile tests and comparison to information provided by the manufacturer.

	Ultimate tensile strength [MPa]	Ultimate straining [%]	Young's modulus [MPa]
Kapton 50 µm	259	68	3400
Upilex 50 µm	352	29	8700
Kapton 50 µm (Producer) [36]	231	72	2760
Upilex 50 µm (Producer) [37]	460	50	9300
Upilex 125 µm (Producer) [37]	340	60	7600

4.2 Thin Film Structure

Fig. 4.3 displays the results of the structural analysis of the thin films deposited by HiPIMS, where only peaks of the thermodynamically stable body-centred cubic and face-centred cubic phase structure of pure Mo and Cu, respectively, can be found. Other peaks that could be assigned to additional phases like nitrides or oxides are absent. The recorded peaks are rather broad indicating the presence of small grains with a size of a few nanometres.

Fig. 4.4 shows the diffractograms recorded from Cu films deposited by HiPIMS and DCMS. The peaks of the Cu films prepared by DCMS are narrower in shape, indicating a higher grain size in this film than in the one deposited by HiPIMS. Further, according to the patterns all deposited Cu films show that they were of cubic structure and polycrystalline. The Cu films have mixed crystalline orientations of (111), (200) and (220) with (111) as the more preferred one, especially for Cu films deposited by HiPIMS. A possible explanation for this might be that the most stable configuration for face-centred cubic lattice is in (111) direction, which retains the lowest surface energy [38].

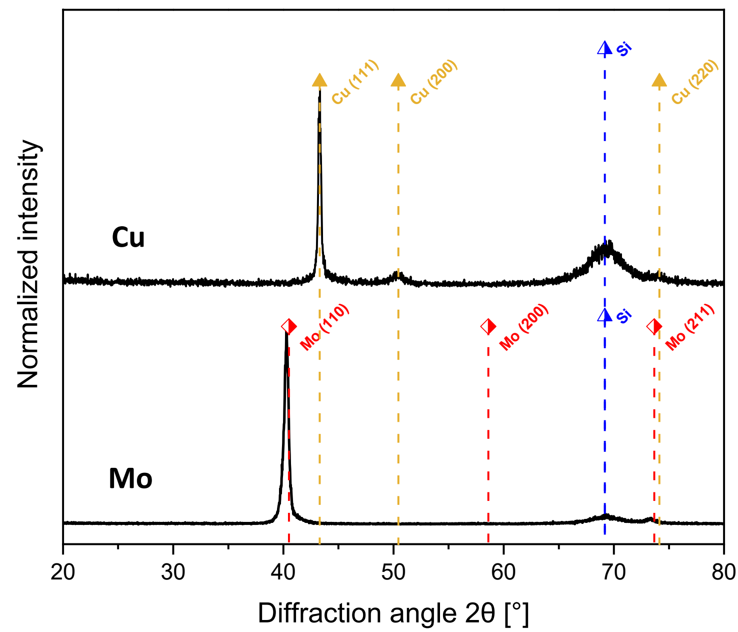

Fig. 4.3: XRD patterns for Cu and Mo films on Si plates deposited by HiPIMS [39-41].

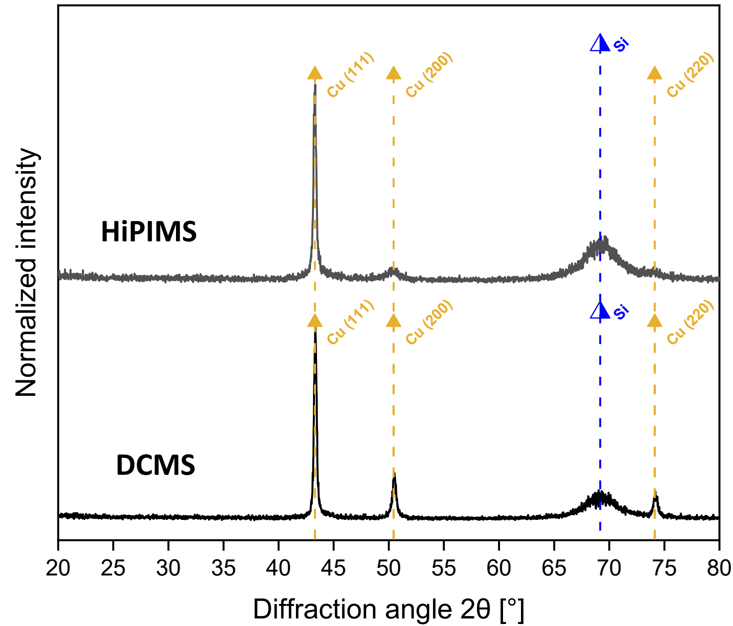

Fig. 4.4: XRD patterns for Cu films on Si plates deposited by HiPIMS and by DCMS [39, 41].

4.3 Electromechanical Behaviour of the Thin Films

4.3.1 Mo films deposited by HiPIMS

As described in Chapter 3, the in-situ 4-point probe resistance measurements were carried out while uniaxially straining the specimens during the tensile test. In Fig. 4.5a the normalized resistance R/R_0 of the Mo films is depicted, where the Mo films were deposited on two different polyimide substrates with a thickness of 125 µm. While straining the Mo films on the polyimide substrates, at 10 % engineering strain a significant larger normalized resistance for Upilex is found compared to Kapton. After unloading, there is still a difference concerning the remaining R/R_0 values for the two polyimide substrates which are higher in the case of Mo films on Upilex. During the unloading process, the normalized resistance shows an unsteady behaviour concerning the expected decrease as it actually increases slightly at strain values of about 6%. This phenomenon is observed especially for the case of Kapton. In Fig. 4.5b the resistance's deviation of the films from the theoretical increase due to the straining of the substrate is depicted. Hence, the COS of the Mo films on 125 µm substrates can be determined at 0.5% engineering strain for Kapton and 1.25% engineering strain for Upilex. This is representative for a brittle behaviour and corresponds to the literature [3].

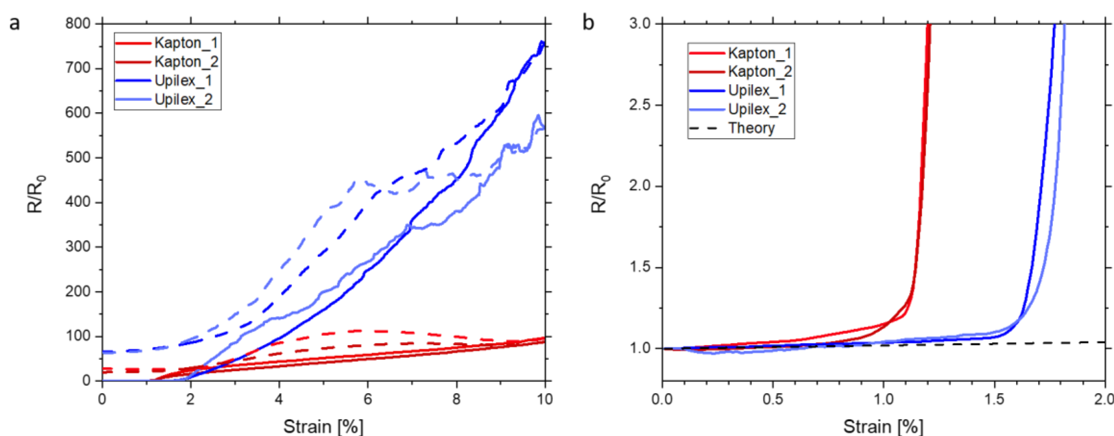

Fig. 4.5: a) Normalized electrical resistance R/R_0 of 300 nm thick Mo films on 125 µm polyimide substrates (Kapton, Upilex) as a function of engineering strain (solid line: loading, dashed line: unloading) during tensile tests. **b)** Magnified view of the measured resistance and the theoretical evolution of the resistance.

Comparing Figs. 4.5a and 4.6a, it can be noticed that the measured normalized resistance with increasing strain is higher for the Mo films that were deposited on a 50 µm thick substrate. At maximum engineering strain the normalized resistance growth of those films on Upilex is considerably higher than for those on Kapton. However, during unloading it is apparent that the expected decrease in resistance is not monotonic again, especially for the Mo film on Upilex. A slight increase is occurring recurrently at about 6% engineering strain. This was also investigated in the case of Mo films on the thicker substrates (see Fig. 4.5a). The remaining resistance after unloading stays at high values for films on Upilex. Using Fig. 4.6b, the COS values for the different polyimides can be determined: 0.25% for Kapton, 0.65% for Upilex. Comparing this to the COS values gained above from Fig. 4.5b, it appears the thinner substrates promote a lower COS.

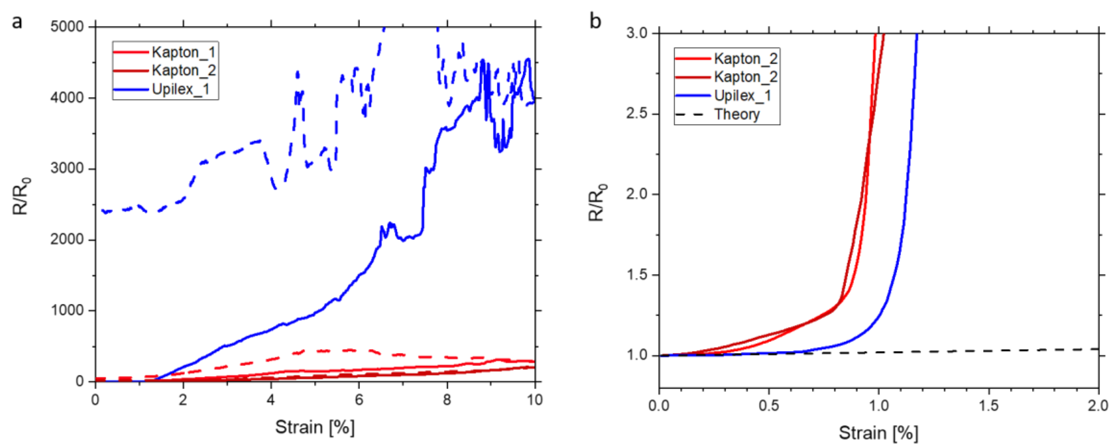

Fig. 4.6 a) Normalized electrical resistance R/R_0 of 300 nm thick Mo films on 50 µm polyimide substrates (Kapton, Upilex) as a function of engineering strain (solid line: loading, dashed line: unloading) during tensile tests. **b)** Magnified view of the measured resistance and the theoretical evolution of the resistance.

The optical information obtained during tensile testing of the Mo films on Kapton is shown in Fig. 4.7. Prior to straining, no cracks are visible on the surface of the Mo films. It is important to note that the Mo films on Kapton reveal a surface roughness which is higher than the one on Upilex (cf. Fig. 4.8). At 0.5% engineering strain first cracking or structural modifications occur. This corresponds well with the investigated COS obtained from the in-situ resistance measurement. At about 10% engineering strain no new cracks are formed, only the existing ones are widened during further straining up to the maximum of 16%. The cracks, that are formed, are straight through-thickness cracks, which is another characteristic attribute for brittle behaviour [4]. In some places, buckles are formed parallel to the straining direction. These buckles appear to be broken in most cases due to the brittle nature of the Mo film. After

unloading, some of the cracks seem to have closed again. In this way more paths are available for the electrical current to flow and the resistance decreases as mentioned above.

Fig 4.8 shows the optical images of the Mo film on the 50 µm Upilex substrates. In a similar way, there are no cracks visible in the as-deposited state of the film. First cracks appear at 1% engineering strain which are straight and perpendicular to the straining direction. As expected for brittle behaviour, the cracks formed in the films are through-thickness cracks [4]. The higher COS of the Mo film on Upilex could be understood by the higher Young's modulus of Upilex, which provides a better support for the Mo film to resist the formation of cracks during straining. At higher strain rates more cracks are formed, and buckles appear as can be seen at the maximum engineering strain of 16%. After unloading, the width of the cracks is reduced and some of them seem to be closed again. When the engineering strain reaches a value below the internal compressive strain in the film cracks are closing and the electrical resistance decreases almost to its initial level. This closure effect is different for every conducted measurement as various local factors influence its outcome [42].

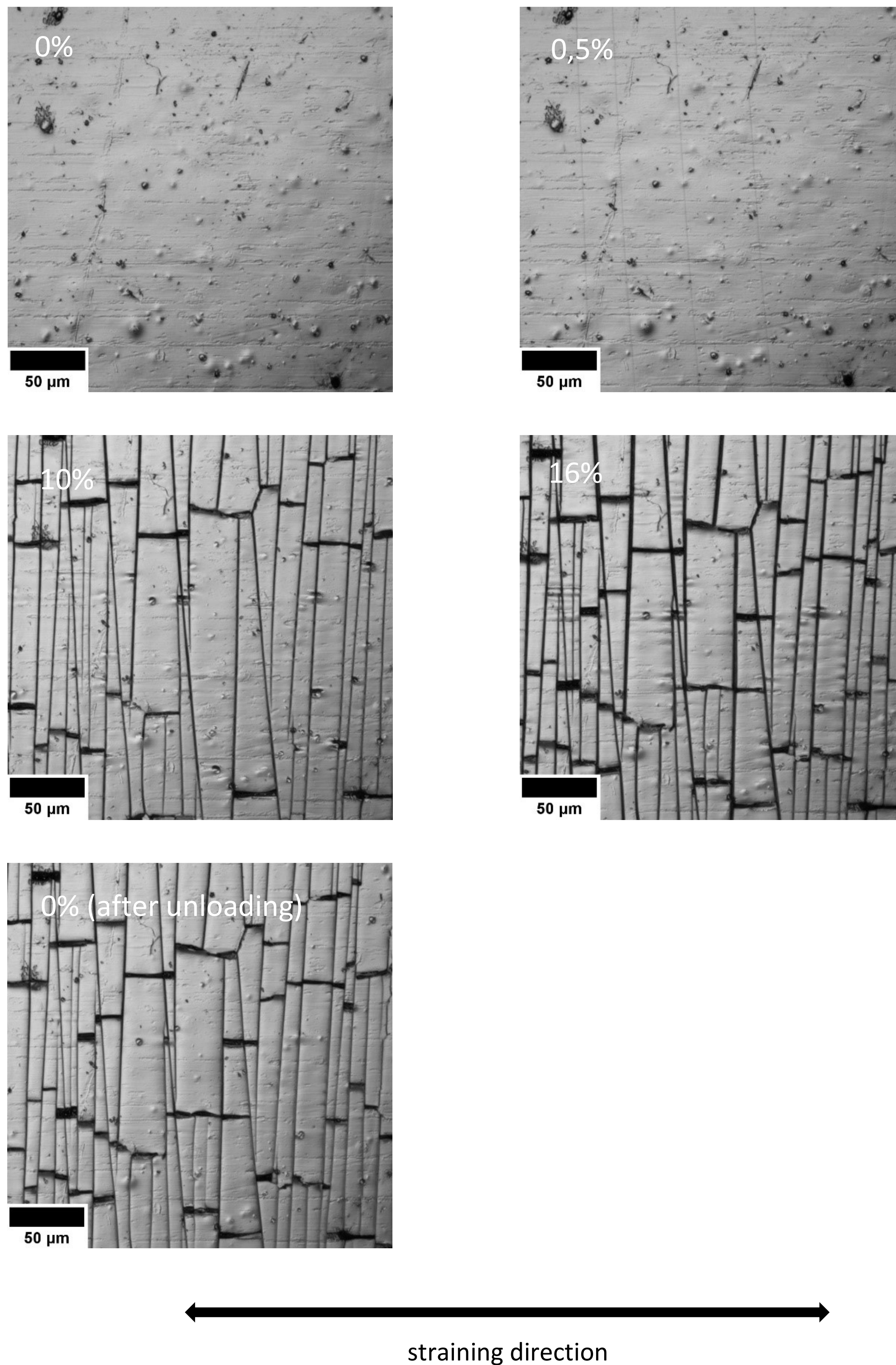

Fig. 4.7: Confocal laser scanning microscope images of a 300 nm Mo film on 50 µm Kapton substrates recorded at different engineering strains during a tensile test.

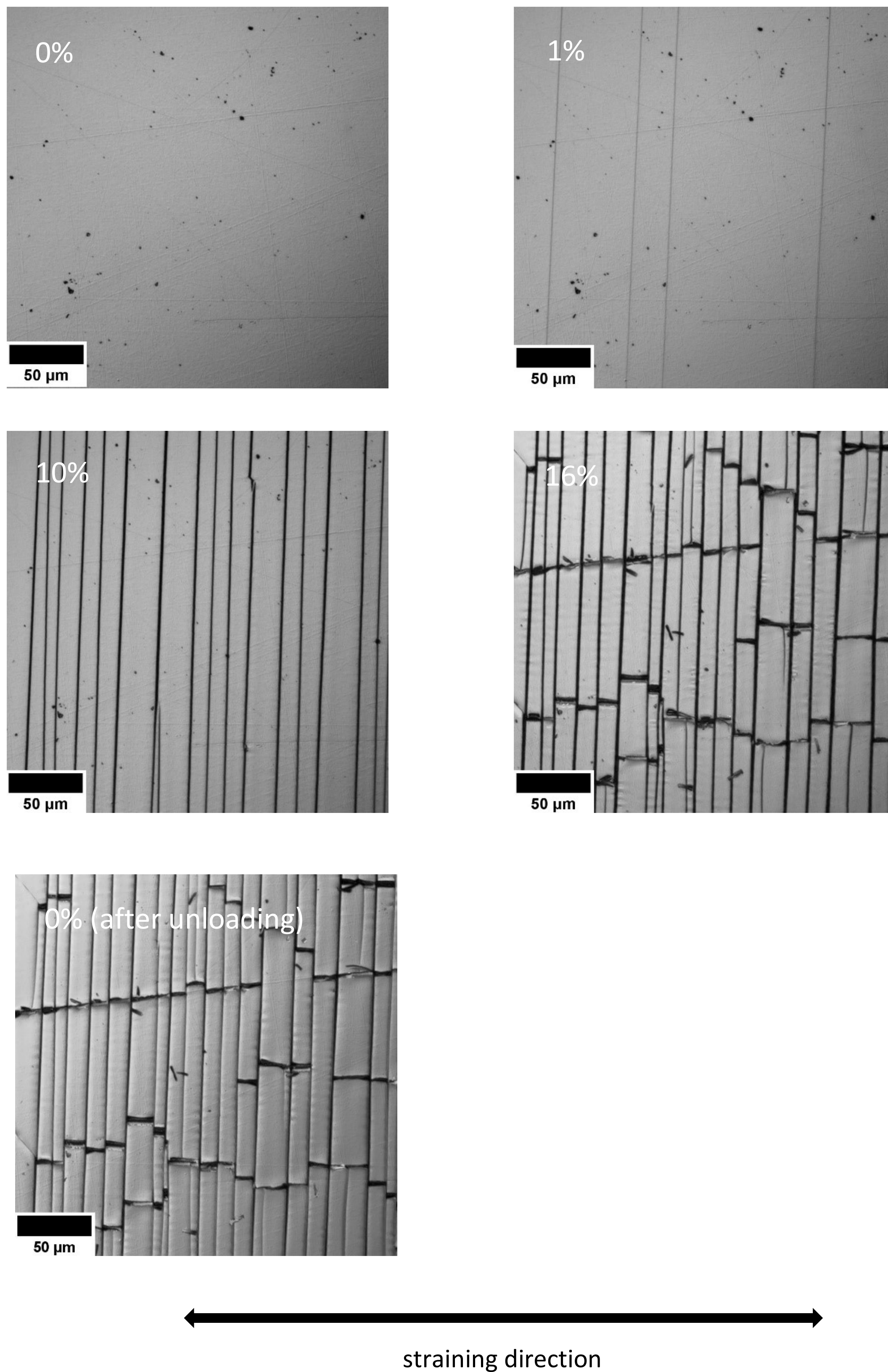

straining direction

Fig. 4.8: Confocal laser scanning microscope images of a 300 nm Mo film on 50 µm Upilex substrates recorded at different engineering strains during a tensile test.

The recorded optical images can be used to determine the crack density of the Mo films which is plotted in Fig. 4.9 together with the recorded resistance values during the tests performed under the confocal laser scanning microscope. The rise of electrical resistance coincides with the increase in crack density. According to Fig. 4.9, the resistance of the Mo films on Kapton and on Upilex starts to increase at 0.5 and 1 % engineering strain, respectively, which correlates well with the values mentioned above. The crack density reaches a saturation at about 10% engineering strain for both films. The final values of the measured crack density are 0.08 μm^{-1} for Kapton and 0.07 μm^{-1} for Upilex.

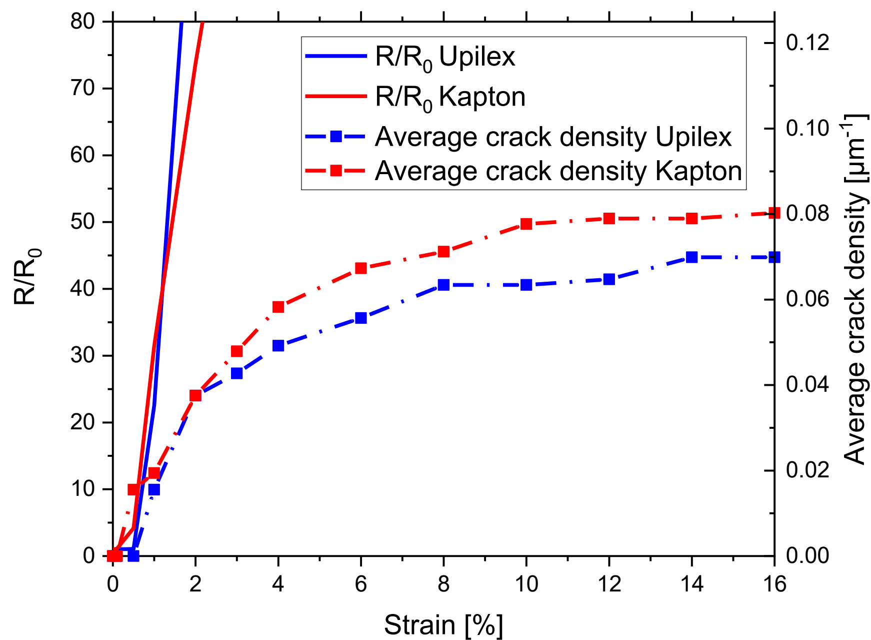

Fig. 4.9: Normalized resistance R/R_0 and average crack density as a function of strain for 300 nm Mo films on 50 µm polyimide substrates (Kapton, Upilex).

4.3.2 Cu films deposited by HiPIMS

Similar to the Mo films, also Cu films with a thickness of 300 nm were deposited by HiPIMS on the same polyimide substrates. Their electromechanical behaviour was also analysed via in-situ tensile tests. Fig. 4.10a shows a comparable normalized resistance growth for both films on Kapton and Upilex at a maximum engineering strain of 10%. During unloading, the resistance is rising in the range of 5 to 6% engineering strain while using Cu films on Kapton substrates. The remaining normalized resistance at unloaded conditions is in similar range again for each film on both polyimides. Fig. 4.10b depicts the development of the normalized resistance R/R_0 of the 300 nm Cu films on 125 µm substrates at low strain, which hence can

be used to determine the COS values of the deposited films. The COS for the Cu films on Kapton during tensile testing is at 0.7%, for Upilex it is higher with a value of 1.9%.

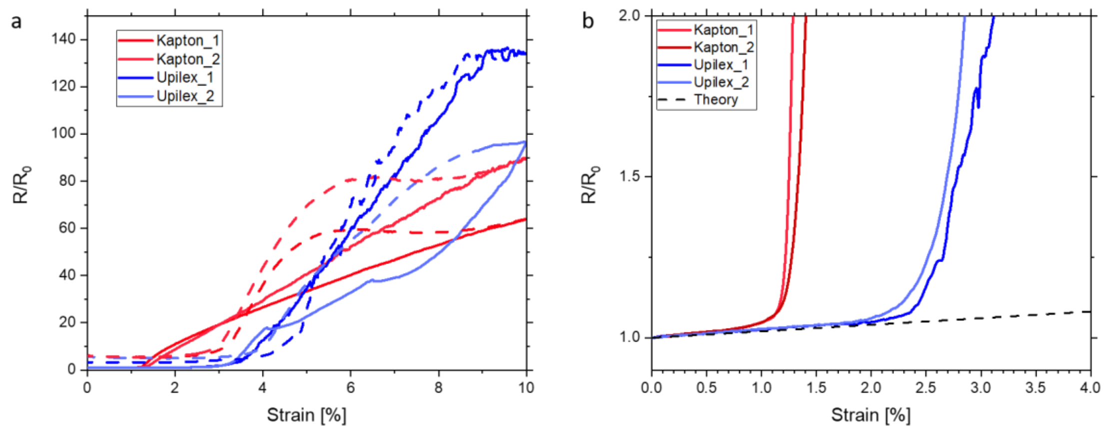

Fig 4.10: a) Normalized electrical resistance R/R_0 of 300 nm thick Cu films on 125 µm polyimide substrates (Kapton, Upilex) as a function of engineering strain (solid line: loading, dashed line: unloading) during tensile tests. **b)** Magnified view of the measured resistance and the theoretical evolution of the resistance.

As it was the case for the Mo films, the same phenomenon concerning the increasing resistance is discovered for the Cu films deposited on thinner Upilex substrates. At maximum strain the measured resistance values for the films on the Upilex substrates are rising compared to the thicker ones, whereas the values of the Cu films on Kapton do not differ significantly (see Fig. 4.11a). Further, during unloading the resistance of the Cu films increases at strain values from 5 to 6%. Such behaviour was already investigated for the Mo films as described above. If Upilex is used, such a behaviour is only found for the Cu films deposited on the thinner substrate having a thickness of 50 µm. However, the increase in resistance is much steadier compared to the Mo film on the thinner Upilex polyimide (cf. Fig. 4.6a). After straining the Cu films show a rather large difference in the remaining normalized resistance. Here, the values for the films on Kapton remain quite similar to the thicker substrates, while the ones on Upilex increase strongly. Such behaviour was already noticed for the Mo films, which can be related to the higher Young's modulus of the Upilex substrate that was only 50 µm thick in comparison to that one with a thickness of 125 µm [37]. The COS of the Cu films varies as the substrate thickness is changed, which is shown in Fig. 4.11b. Comparing Figs. 4.10b and 4.11b it is evident that the COS values obtained for the thinner Kapton and Upilex substrates are significantly lower with values of 0.45% and 1.0% than those for the 125 µm thick substrates.

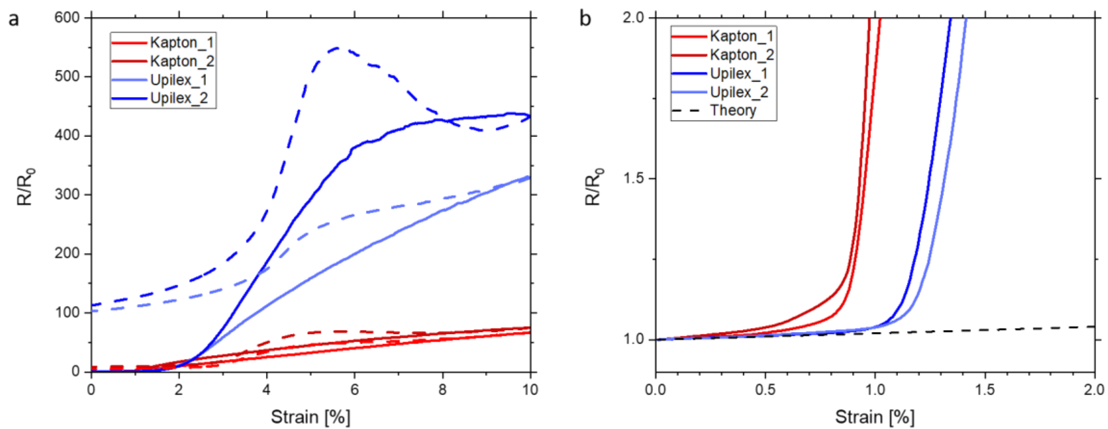

Fig 4.11: a) Normalized electrical resistance R/R_0 of 300 nm thick Cu films on 50 µm polyimide substrates (Kapton, Upilex) as a function of engineering strain (solid line: loading, dashed line: unloading) during tensile tests. **b)** Magnified view of the measured resistance and the theoretical evolution of the resistance.

The electromechanical behaviour of the Cu films on a 50 µm thick substrates were also analysed by in-situ optical measurements, as mentioned in the previous section. Comparing Fig. 4.12, which shows the Cu films on 50 µm thick Kapton to Fig. 4.13 where Upilex with the same thickness was used, it can be noticed again, that the surface on Kapton is rougher than on Upilex. This can be assumed since a high number of spots is visible on the film surface in the case of Kapton. The first cracks appear at an engineering strain of 0.5%, perpendicular to the straining direction, which corresponds well with the information obtained from measuring the resistance. Straight through-thickness cracks are characteristic for brittle behaviour [4] and show a result that was not anticipated since ductile behaviour was expected for the deposited Cu films [43]. However, the rise in electrical resistance of the Cu films, which was mentioned beforehand, corresponds to brittle behaviour [42]. This is an uncharacteristic behaviour, especially for the COS values which are seen at such low engineering strain. At about 10% engineering strain the cracks are widened and appear closed after the unloading cycle to 0% engineering strain. This correlates with the strong decrease in resistance described above.

Fig 4.13 shows the optical images of the Cu film on the 50 µm Upilex substrates. No cracks are visible in as-deposited state of the film. Similar to Mo films on 50 µm Upilex polyimide, first cracks appear at 1% engineering strain which are straight through-thickness cracks, perpendicular to the straining direction. Again, this is a rather unexpected behaviour of Cu films. The higher COS of the Cu film on Upilex is probably related to the higher Young's modulus of Upilex, as it was already discussed for the Mo films. At higher engineering strain

more cracks arise, but after 10% engineering strain no significant formation of cracks is witnessed until the maximum strain of 16% is reached. The cracks of the Cu film appear more closed if Upilex substrate is used rather than Kapton. This discovery can also be assumed to correlate with the overall higher Young's modulus of the Upilex polyimides. No buckles appear even at maximum strain, though. After unloading, the width of the cracks is reduced and some of them appear to be closed again.

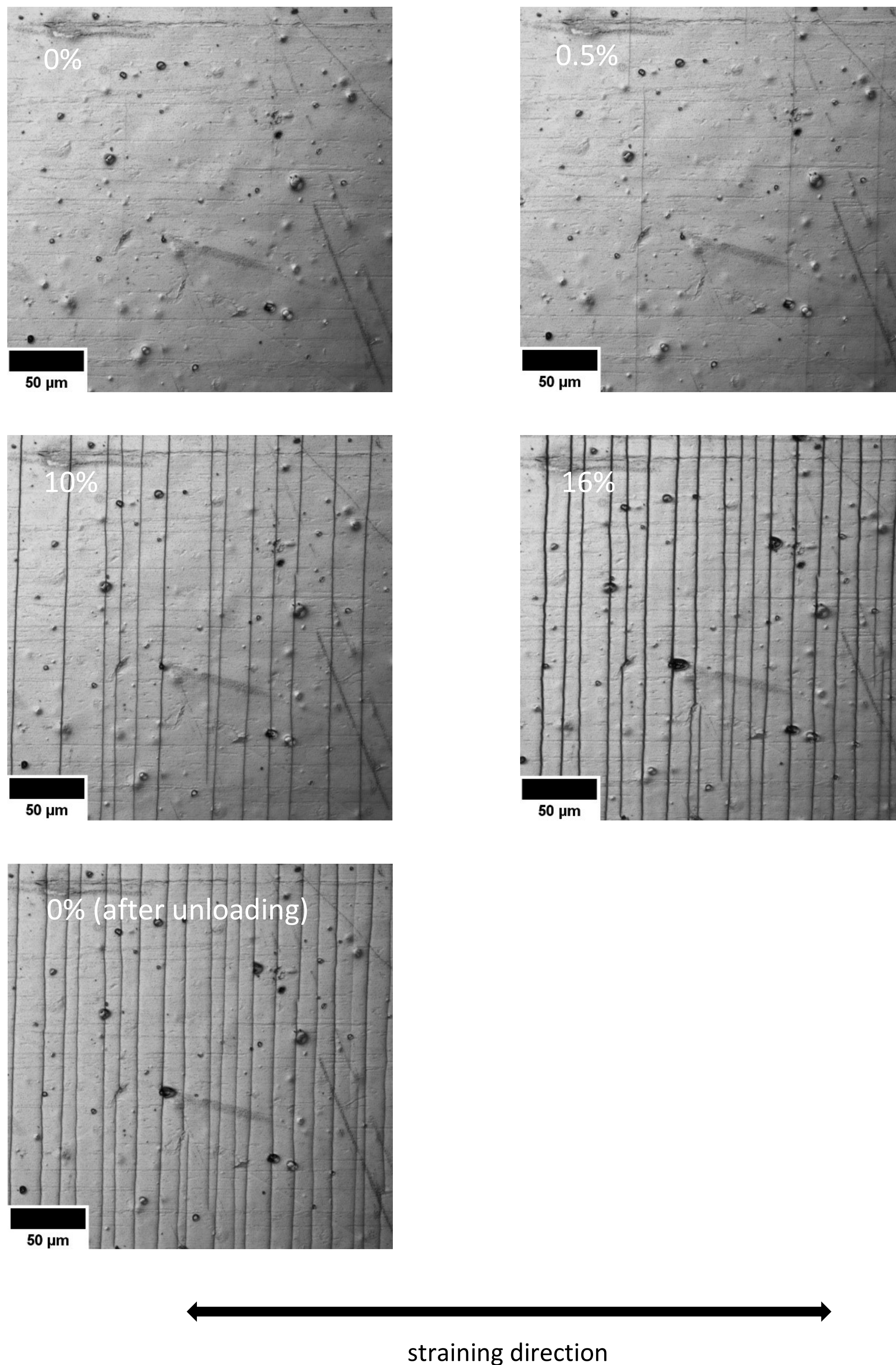

Fig. 4.12: Confocal laser scanning microscope images of a 300 nm Cu film on 50 µm Kapton substrates recorded at different engineering strains during a tensile test.

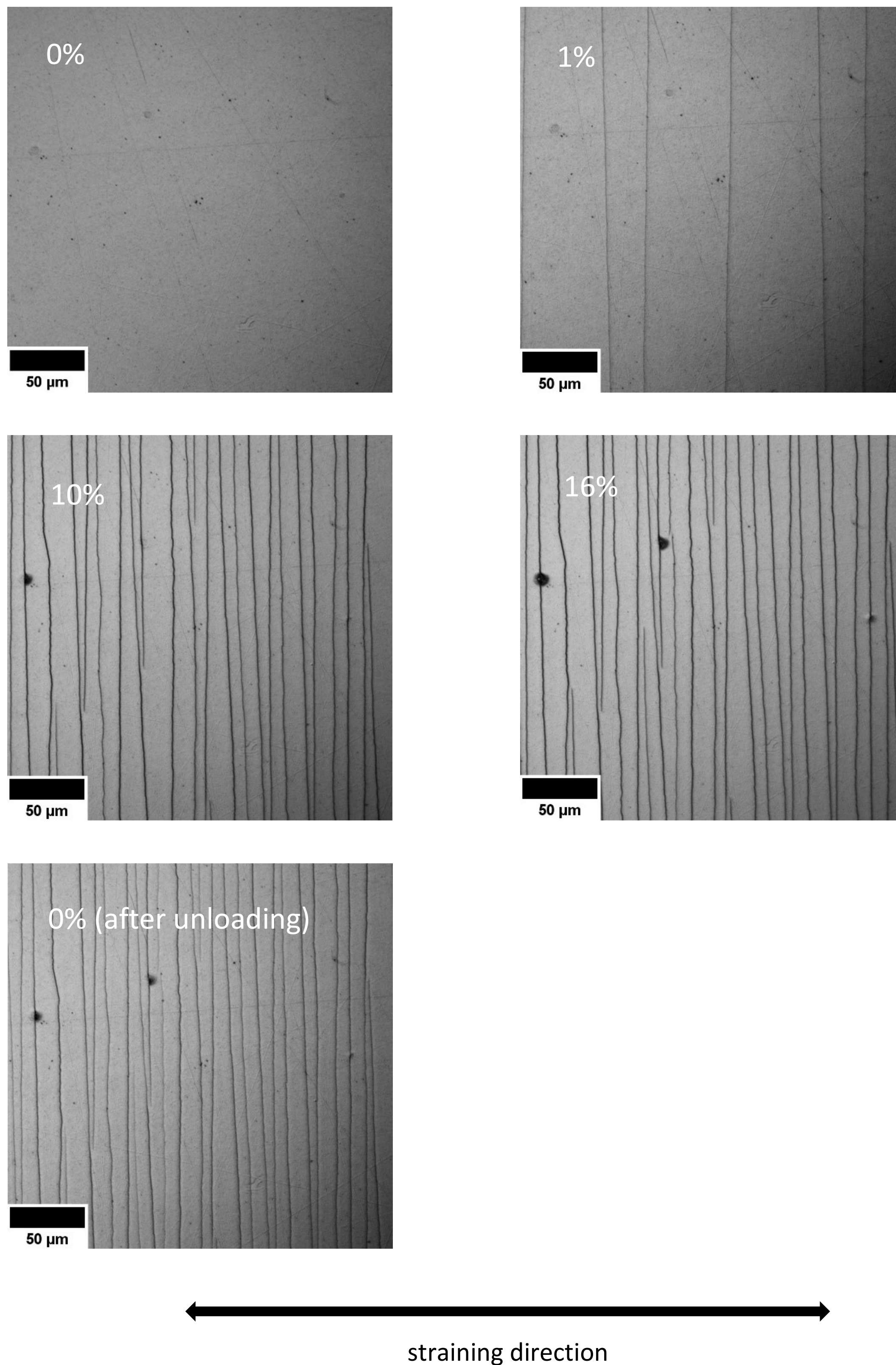

Fig. 4.13: Confocal laser scanning microscope images of a 300 nm Cu film on 50 µm Upilex substrates recorded at different engineering strains during a tensile test.

The crack density determined from the recorded optical images and the electrical resistance as a function of engineering strain are presented in Fig. 4.14. The rising of the electrical resistance as well as the rising of the crack density occur at similar values of the strain for each polyimide. Since the resistance of the Cu films on Kapton and Upilex increases from 0.5 and 1% engineering strain, respectively, it is obvious that these values are in good agreement with the ones mentioned above. The crack density reaches a saturation at about 10% engineering strain for both films similar to the Mo films. At 16% engineering strain, the crack density has the values of 0.07 μm^{-1} for Kapton and nearly 0.1 μm^{-1} for Upilex. The saturated crack density of the Cu films on Kapton is nearly the same as the one for the Mo films on Kapton. However, this is not the case for the Cu films on Upilex substrates since their density does significantly increase which can be seen in Fig. 4.9.

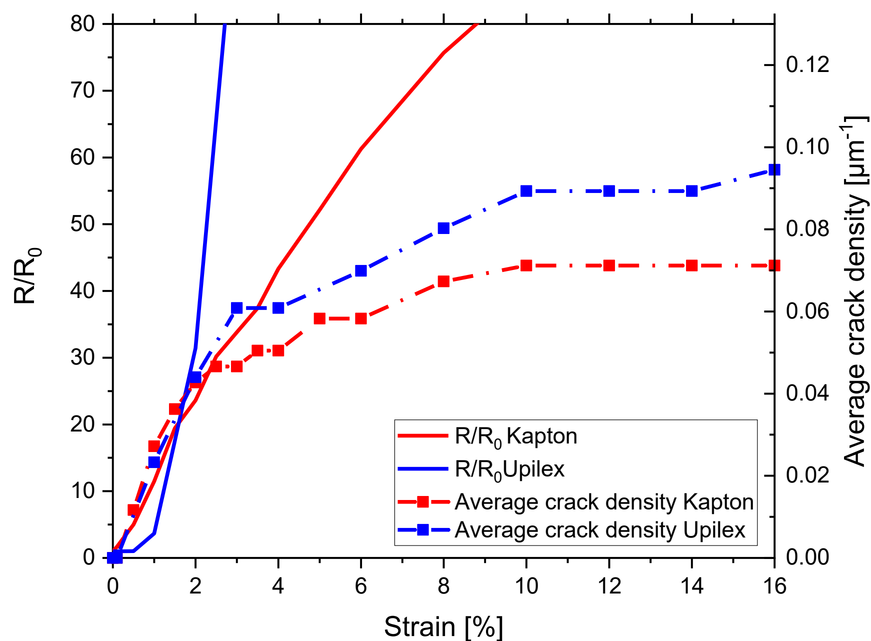

Fig. 4.14: Normalized resistance R/R_0 and average crack density as a function of strain for 300 nm Cu films on 50 µm polyimide substrates (Kapton, Upilex).

In an attempt to further investigate such unexpected brittle behaviour of the Cu films, SEM investigations of the strained and relieved samples on the 50 µm thick substrates were performed. Looking at Fig. 4.15, the pronounced nanocrystalline microstructure might be the explanation for the observed brittle behaviour. Since the cracks start appearing between the crystallites, they can only follow the grain boundaries. This is a consequence of the restricted ductility by the small grain size of the nanocrystalline structure [44,45]. Moreover, the cracks differ greatly from each polyimide investigated, e.g. the cracks on Kapton are closed for the

main part, those on Upilex seem to stay open. This behaviour leads to the vast difference of resistance after unloading in the in-situ tensile tests mentioned before (cf. Fig. 4.11).

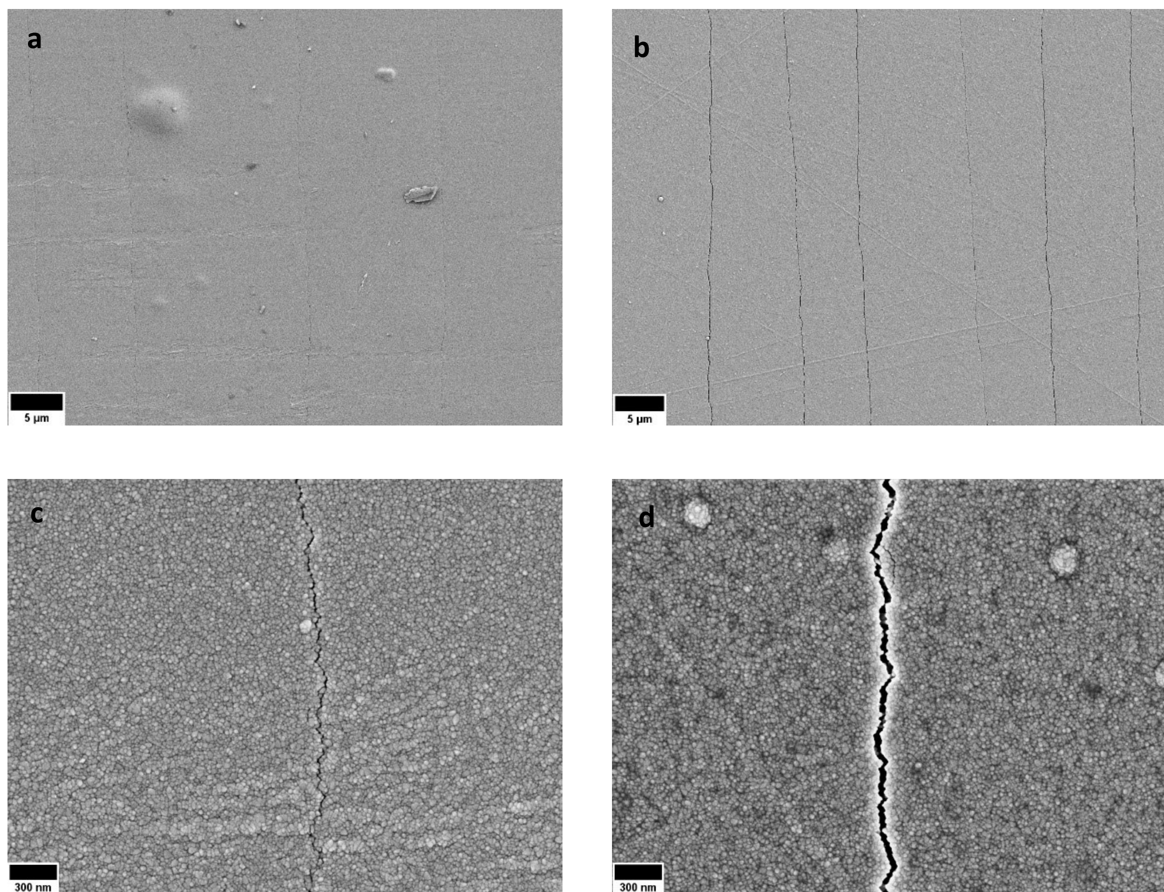

Fig 4.15: SEM images of the surface of a 300 nm Cu film on (a) 50 µm Kapton substrates and (b) 50 µm Upilex substrates in unloaded state after straining. The pictures (c) and (d) show higher magnified images of cracks from (a) and (b) respectively.

This is in accordance to the measurements done with the thicker substrates of 125 µm (see Fig. 4.16) as the cracks are less visible and therefore their electrical resistances are more similar to each other (cf. Fig. 4.10).

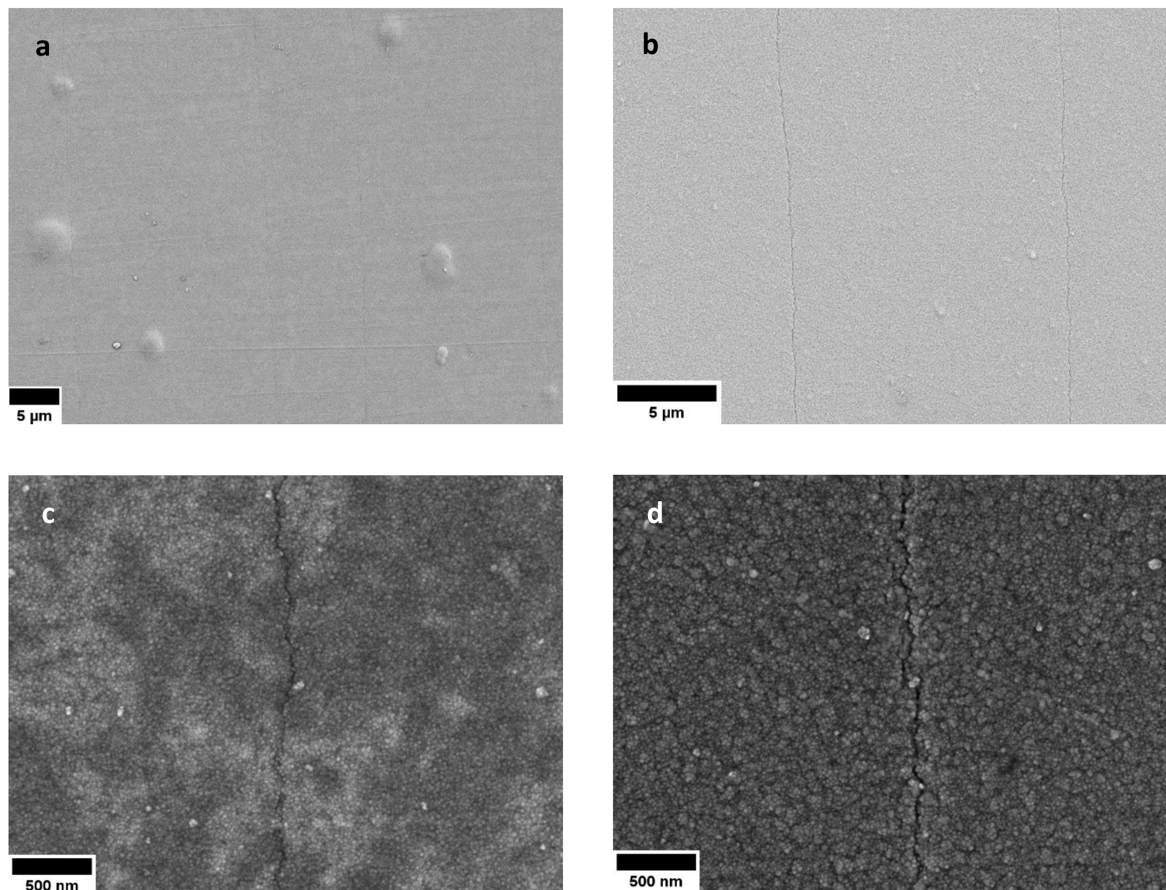

Fig 4.16: SEM images of the surface of a 300 nm Cu film on (a) 125 µm Kapton substrates and (b) 125 µm Upilex substrates in unloaded state after straining. The pictures (c) and (d) show higher magnified images of cracks from (a) and (b) respectively.

4.3.3 Cu films deposited by DCMS

According to the previous section, it was found that Cu films deposited by the HiPIMS process are more prone to brittle behaviour. This was rather unexpected as Cu is a material known to behave more ductile [43]. Therefore, another series of Cu films was deposited by the DCMS process. Compared to the HiPIMS deposition process, the conditions for the growing films were less energetic during DCMS and therefore it was expected, that larger grains are forming which leads to a more ductile behaviour of the films. According to film thickness measurements, the films were a little thicker with a thickness of about 500 nm. As shown in Fig. 4.17a, the normalized electrical resistances measured for the Cu films on 125 µm thick Kapton are marginally higher than those on Upilex at the applied maximum engineering strain of 10%. While the values for the resistance are rather similar for those Cu films that were deposited by HiPIMS on Kapton, the resistance growth of the Cu films deposited on Upilex polyimide is severely reduced which is indicating possibly a more ductile behaviour. After

unloading to 0% engineering strain, the remaining electrical resistance is slightly higher than the resistance of the HiPIMS Cu films after tensile straining regardless of the used polyimide substrate material. The COS is determined at 0.2% engineering strain for the Cu films on Kapton and at 0.8% for the Cu films on Upilex (see Fig. 4.17b). Although a more ductile behaviour seems to be present, the COS values for the Cu films deposited by the DCMS process are significantly lower than those achieved by the HiPMS deposited Cu films (see Fig. 4.10b). A possible explanation might be the expected higher level of compressive stress in the Cu films deposited by HiPIMS which causes higher COS values in tensile testing [3].

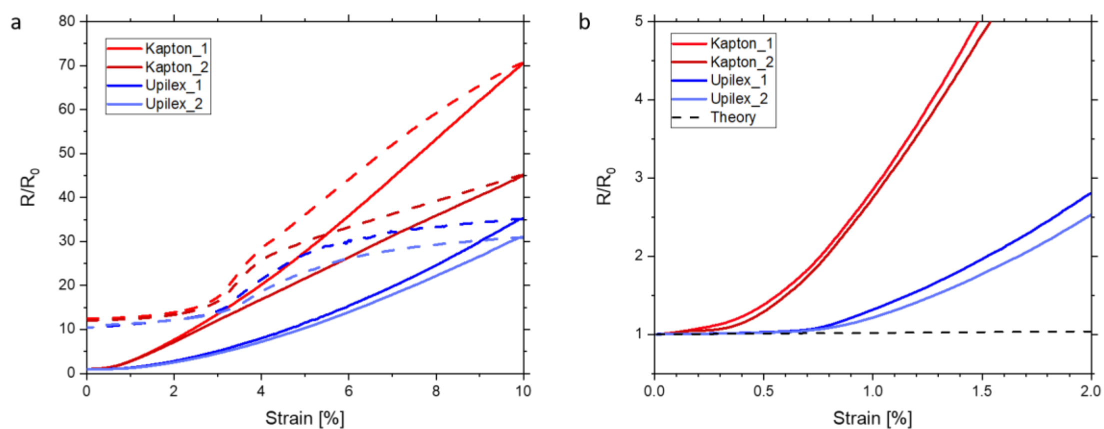

Fig 4.17: a) Normalized electrical resistance R/R_0 of 500 nm thick Cu films deposited by HiPIMS on 125 µm polyimide substrates (Kapton, Upilex) as a function of engineering strain (solid line: loading, dashed line: unloading) during tensile tests. **b)** Magnified view of the measured resistance and the theoretical evolution of the resistance.

If the substrate thickness is reduced to 50 µm, the normalized electrical resistance in Fig. 4.18a shows a very different outcome to the one with a higher substrate thickness. The normalized resistance at 10% engineering strain is detected at similar values for both Cu films deposited on Kapton substrates. In comparison, the values determined for Upilex are significantly lower. Comparing the values of the electrical resistance between the HiPIMS process and the DCMS process, it can be noticed that the value at the maximum engineering strain of 10% drops strongly for the Cu films on Upilex when changing from HiPIMS to DCMS. Only a very moderate resistance growth can be observed for DCMS Cu films followed by a strong decrease in resistance after unloading compared to HiPIMS films. Hence, a ductile behaviour of the DCMS Cu films on Upilex can be assumed. The remaining resistances of the DCMS deposited Cu films on Kapton polyimides are little higher than those obtained for the HiPIMS films. As shown in Fig. 4.18b, the COS for the Cu films on Upilex is at about 1% engineering strain, which shows no great difference to the COS of the Cu films deposited by HiPIMS. Since the COS of the Cu

films on Kapton is near 0% engineering strain, there is an almost immediate rise in electrical resistance right after the start of the tensile straining. It seems that the change in substrate thickness hardly influences the electromechanical behaviour of the Cu films on Kapton since the results are quite similar. However, if Cu films on Upilex substrates are investigated, the influence of the changing thickness as well as the used deposition process becomes quite clear. If HiPIMS Cu films are used, a rise in the electrical resistance can be seen during straining which becomes more prominent when the substrate thickness is reduced. This is in contrast to the DCMS Cu films since those films on 50 µm Upilex tend to a rather ductile behaviour as indicated by the electrical resistance evolution while straining.

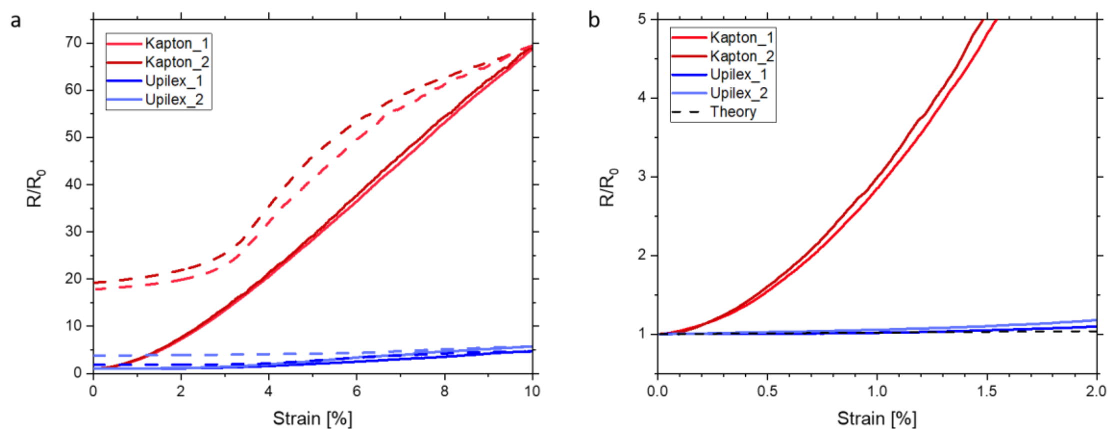

Fig 4.18: a) Normalized electrical resistance R/R_0 of 500 nm thick Cu films deposited by HiPIMS on 50 µm polyimide substrates (Kapton, Upilex) as a function of engineering strain (solid line: loading, dashed line: unloading) during tensile tests. **b)** Magnified view of the measured resistance and the theoretical evolution of the resistance.

The Cu films on Upilex were further investigated using in-situ optical tensile tests, where the results are shown in selected optical images in Fig. 4.19. Upon closer inspection, a difference in their surface is visible as the surface of the Cu films deposited by DCMS is rougher than the one of the Cu films deposited by HiPIMS (see Fig. 4.13). The first cracks appear at an engineering strain of 2% perpendicular to the straining direction. The formed cracks are shorter than those discovered on the HiPIMS films that tend to more brittle behaviour. Since the cracks' growth is limited, the electrical current can use various paths which significantly lowers the rise of electrical resistance. At about 10% engineering strain there is no further development of cracks even though the straining continues. Towards the maximum of 16% the expansion of the cracks is observed, but at the same time also the closure of some during the unloading process.

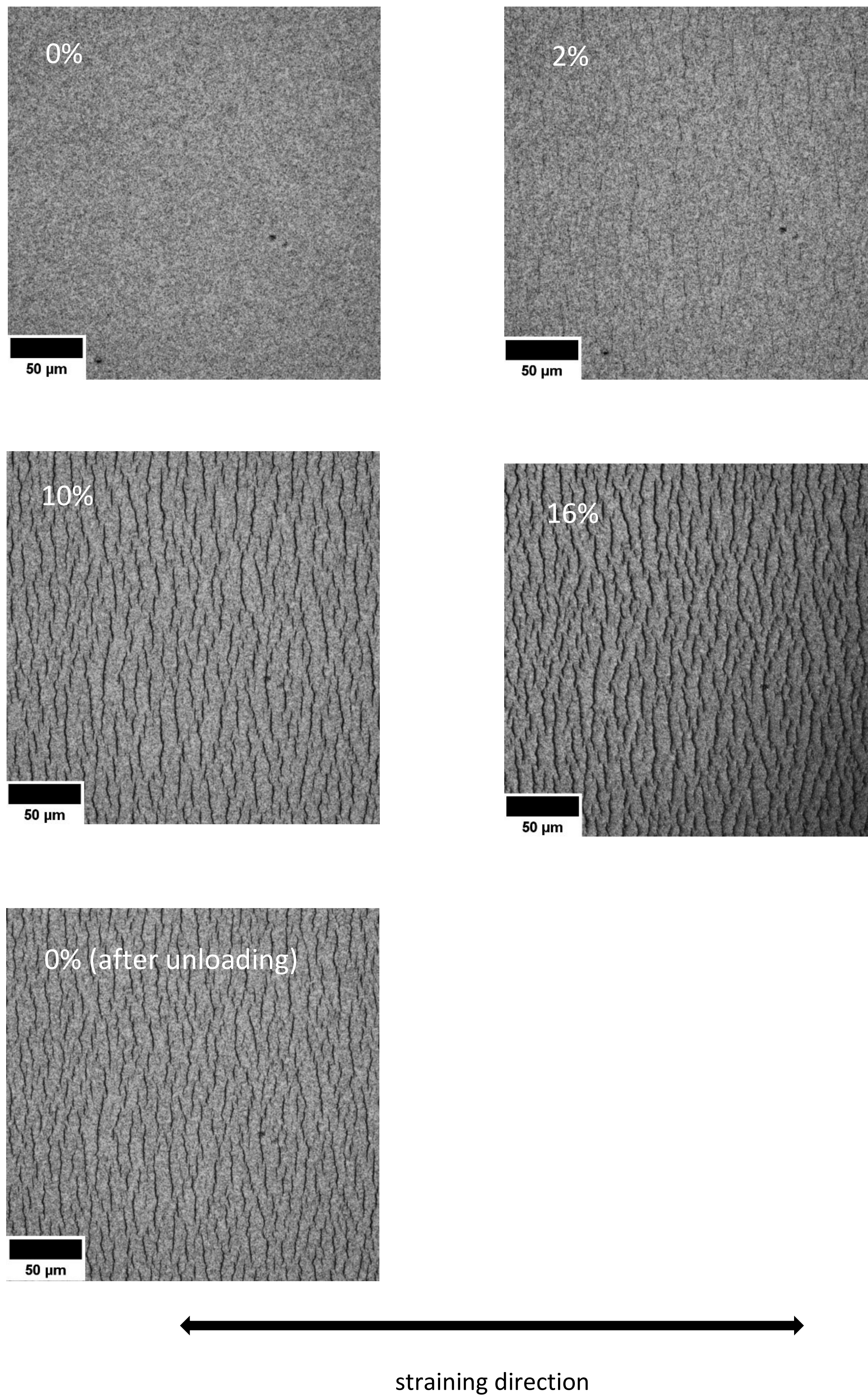

Fig. 4.19: Confocal laser scanning microscope images of a 500 nm Cu film on 50 µm Upilex substrates recorded at different engineering strains during a tensile test.

The crack density determined from the recorded optical images and the normalized electrical resistance as a function of the engineering strain is presented in Fig. 4.20 as well as the values obtained from the HiPIMS Cu films. According to the graph, the onset of the electrical resistance of the DCMS films occurs at about 2% engineering strain which happens later than for the HiPIMS Cu films. The crack density starts to saturate at about 10% engineering strain and reaches a value of about 0.1 μm^{-1} at the maximum engineering strain of 16%. This value is slightly higher than the values investigated for HiPIMS Cu films on Kapton and Upilex.

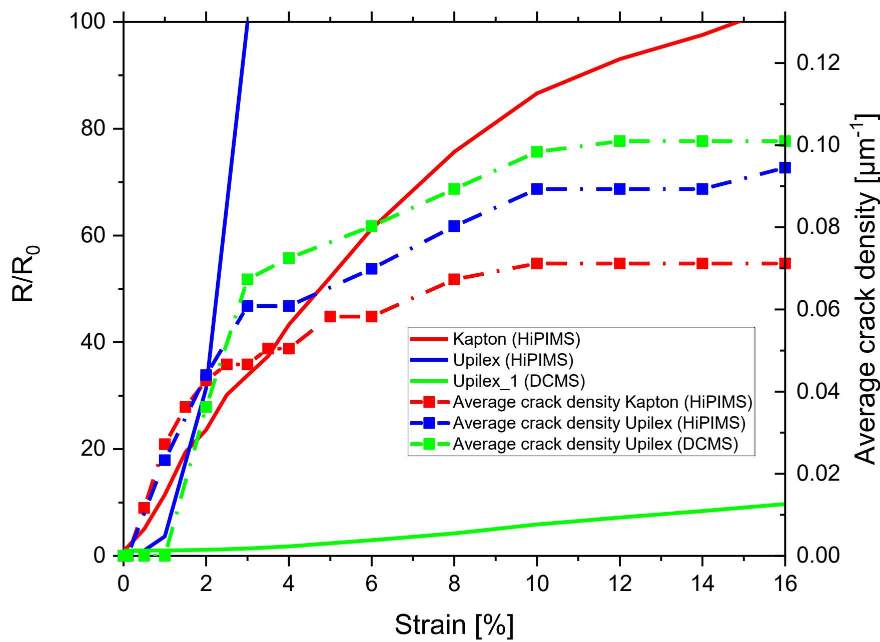

Fig. 4.20 Average crack density as function of strain for 500 nm Cu films deposited by DCMS on 50 µm substrates (Upilex) compared to 300 nm Cu films deposited by HiPIMS on 50 µm substrates (Kapton,Upilex).

In Fig 4.21, SEM pictures of the modifed Cu film are depicted. As it can be seen, the film consists of interconnected nanoparticels and pores. The cracks appear rather short compared to the HiPIMS Cu film. Overall the film looks like an ink-jet film made on nanoparticle based ink [46].

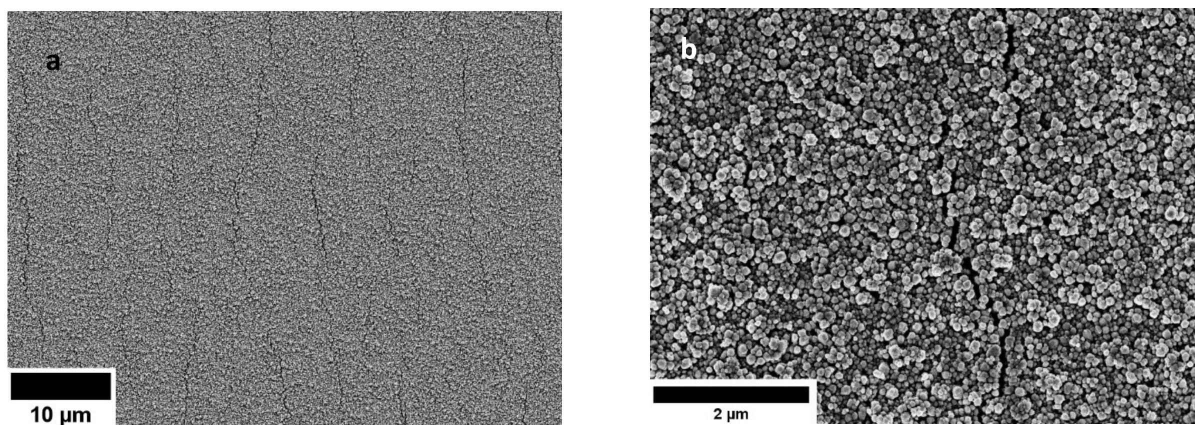

Fig 4.21: SEM images of a 500 nm Cu film on a) b) 50 µm Upilex substrates in unloaded state after straining in different magnification.

5 Summary and Conclusions

A comparative study of the influence of different polyimide substrates (DuPont Kapton, UBE Industries Upilex) and their thicknesses on the electromechanical behaviour of Mo and Cu metallic films was carried out within this work. The films were deposited by different PVD techniques including HiPIMS and DCMS. The deposition parameters were carefully chosen to limit thermally induced events within the polyimide substrates due to plasma heating during the deposition process.

The electromechanical behaviour was assessed by tensile tests with in-situ 4 point-probe resistance measurements and/or optical analysis. According to the obtained mechanical characteristics of the polyimides, the electromechanical properties of the thin metallic films are strongly influenced by the choice of the substrate material. In general, the films deposited on Kapton experience an earlier onset of crack formation during straining compared to those on Upilex, but with exception of DCMS Cu films, the overall increase in electrical resistance is higher for films on Upilex. A possible explanation for the higher crack onset strain when using Upilex, could be its higher Young's modulus and ultimate tensile strength which provides a better support for the thin films during straining. In contrast to this, the more pronounced increase in resistance for HiPIMS films on Upilex can be explained by the formation of more through-thickness cracks which are hindering the flow of current throughout the metallic film, as supported through the optical images obtained via confocal laser microscope. After straining, the electric resistance of HiPIMS films on Kapton is lower compared to those on Upilex. Scanning electron microscope investigations show a closure effect for films on Kapton, which can be explained by the higher elastic strain of this polyimide. Further, a higher surface roughness of the films on Kapton was detected. Differential scanning calorimetry measurements of Kapton show a phase transition temperature at about 80 °C, which lies within the measured temperature range of the deposition process. This can lead to the assumption that this phase transition temperature can cause more surface defects on the actual surface of the substrate or within the thin film. Cu films deposited by DCMS on Kapton do not show a significantly change of their electromechanical behaviour compared to those deposited by HiPIMS, with exception of the crack onset strain, which is obtained at smaller values. However, DCMS Cu films deposited on Upilex show a tremendous alteration in electric resistance, as their values reduce strongly.

A rise in values of the electrical resistance for metallic films on thinner polyimides substrates is determined, which seems reasonable, according to less support of the polyimide during straining. The change of electric resistance is more pronounced for films deposited by HiPIMS on Upilex, which show a strong increase, when the thinner substrate is used. For Cu films

deposited by DCMS there is a higher increase of the resistance values on the thicker Upilex polyimide which, somehow, contradicts the overall trend for larger resistance values using thinner substrates. The manufacturer's information for Upilex polyimide show an interesting consequence as the properties differ from each other for diverse thicknesses. This could indicate a different chemical composition, which might affect the outcome during the DCMS deposition process and should be investigated in further research.

In general, it should be noted that each polyimide supports thin metallic films in a different way and have to be used according to its profile. Also, deposition parameters must be chosen carefully as they influence the outcome of the properties, according to the used polyimide, heavily. The right choice of the polyimide and deposition parameter not only for the metallic films but also for the substrate used, consequently, can help to reach further improvements.

6 Literature

1. O. Glushko et al., Recovery of electrical resistance in copper films on polyethylene terephthalate subjected to a tensile strain, Thin Solid Films 552 (2014) 141-145.
2. O. Glushko, M. J. Cordill, Electrical resistance of metal films on polymer Substrates under tension, Experimental Techniques 40 (2016) 303-310.
3. T. Jörg et al., The electro-mechanical behavior of sputter-deposited Mo thin films on flexible substrates, Thin Solid Films 606 (2016) 45-50.
4. M. J. Cordill et al., Measuring electro-mechanical properties of thin films on polymer substrates, Microelectronic Engineering 137 (2015) 96–100.
5. P. Kreiml et al., Electro-mechanical behavior of Al/Mo bilayers studied with in situ straining methods, Thin Solid Films 665 (2018) 131-136.
6. D. Mattox, "Handbook of Physical Vapor Deposition (PVD) Processing", Elsevier, Oxford, 2010.
7. A. Simon, in K. Seshan (ed.) and D. Schepis (ed.), "Handbook of Thin Film Deposition", Elsevier, Oxford, 2018, p. 195-230.
8. P. Martin, "Handbook of Deposition Technologies for Films and Coatings", Elsevier, Oxford, 2010.
9. M. C. Petty, Organic thin film deposition techniques, Encyclopedia of Nanoscience and Nanotechnology 8 (2004) 295-304.
10. D. Smith, "Thin-Film Deposition – Principle and Practice", McGraw-Hill, USA, 1995, p. 1-7.
11. R. Haefer, "Oberflächen und Dünnschicht-Technologie", Springer, Berlin, 1987, p. 95-120.
12. J. Musil, J. Vlcek, P. Baroch, in Y. Pauleau (ed.), "Materials Surface Processing by Directed Energy Techniques", Elsevier, Oxford, p. 67-106.
13. P.J. Kelly, R.D. Arnell, Magnetron sputtering: a review of recent developments and applications, Vacuum 56 (2000) 159 – 172.
14. A. Anders, Discharge physics of high power impulse magnetron sputtering, Surface and Coatings Technology 205 (2011) 1–9.
15. D. A. Golosov, Balanced magnetic field in magnetron sputtering systems, Vacuum 139 (2017) 109-116.
16. K. Sarakinos, J. Alami, and S. Konstantinidis, High power pulsed magnetron sputtering: A review on scientific and engineering state of the art, Surface and Coatings Technology 204 (2010) 1661–1684.

17. V. Kouznetsov, et al., A novel pulsed magnetron sputter technique utilizing very high target power densities, Surface and Coatings Technology 122 (1999) 290-293.
18. P. Sigmund, Theory of sputtering. I. Sputtering yield of amorphous and polycrystalline targets, Physical Review 184 (1968) 383-416.
19. A. Kameneva, Evolution of the film structure in the various evaporation processes, Research Journal of Pharmaceutical, Biological and Chemical Sciences 6 (2015) 951-960.
20. P. B. Barna and G. Radnoczi in K. Barmak (ed.) and K. Coffey (ed.), “Metallic films for electronic, optical and magnetic applications”, Woodhead Publishing, 2014, p. 67-120.
21. B. A. Movchan, A. V. Demshichin, Study of the structure and properties of thick vacuum condensates of nickel, titanium, aluminum and zircon dioxide, Fizika Metallov i Metallovedenie 28 (1969) 83–95.
22. J. A. Thornton, High rate thick film growth, Annual Review of Materials Science 7 (1977) 239-260.
23. A. Lakhtakia and R. Messier, “Sculptured Thin Films – Nanoengineered Morphology and Optics”, SPIE Press, 2005, p. 27-47.
24. J. A. Thornton, Influence of apparatus geometry and deposition conditions on the structure and topography of thick sputtered coatings, Journal of Vacuum Science and Technology 11 (1974) 666-670.
25. Y. Waseda, E. Matsubara and K. Shinoda, “X-Ray Diffraction Crystallography”, Springer, Berlin, 2011.
26. B. D. Culity and S. R. Stock, “Elements of X-Ray Diffraction”, Pearson, London, 2014, p. 91-124.
27. T. Oeser, “Kristallstrukturanalyse durch Röntgenbeugung“, Springer Spektrum, Wiesbaden, 2019, p. 21-23.
28. V. K. Pecharsky and P. Y. Zavalij, “Fundamentals of Powder Diffraction and Structural Characterization of Materials”, Springer, Berlin, 2009, p. 107-132.
29. G. W. H. Höhne, W. F. Hemminger and H. -J. Flammersheim, “Differential Scanning Calorimetry”, Springer, Berlin, 2003, p. 1-30.
30. S. M. Sarge, G. W. H. Höhne and W. Hemminger, “Calorimetry – Fundamentals, Instrumentation and Applications”, Wiley-VCH, Weinheim, 2014.
31. R. Patzelt and H. Schweinzer,“Elektrische Messtechnik“, Springer, Berlin, 1996, p. 321-322.
32. D. C. Agrawal, R. Raj, Measurement of the ultimate shear strength of a metal-ceramic interface, Acta Metallurgica 7 (1989) 1265-1270.

33. V. Georgenthum et al., Influence of outer zirconia transient cracking and spalling on thermomechanical behaviour of high burnup fuel rod submitted to RIA, Journal of Nuclear Science and Technology 43 (2006) 1089–1096.
34. W. Kaiser, “Kunststoffchemie für Ingenieure“, Hanser, München, 2006, p. 440-448.
35. H. Dominighaus, “Die Kunststoffe und ihre Eigenschaften“, Springer, Berlin, 2005, p. 1235-1250.
36. “Du Pont™ Kapton® HN Polyimide Film“ datasheet downloaded from manufacturer’s website www.dupont.com/products/kapton-hn.html (May 2020).
37. “UPILEX®-S” datasheet downloaded from manufacturer’s website www.ube.com/upilex/en/catalog.html#cata_upilex (May 2020).
38. A. A. Solovyev et al., Comparative study of cu films prepared by dc, high-power pulsed and burst magnetron sputtering, Journal of Electronic Materials 45 (2016) 4052-4060.
39. International Centre for Diffraction Data, Cu, 1953, Card no. 00-004-0836.
40. International Centre for Diffraction Data, Mo, 1953, Card no. 00-004-0809.
41. International Centre for Diffraction Data, Si, 1953, Card no. 00-005-0565.
42. Q. Guan et al., Mechanical failure of brittle thin films on polymers during bending by two-point rotation, Thin Solid Films 611 (2016) 107-116.
43. K. M. Gupta, “Engineering Materials – Research, Applications and Advances”, CRC Press, Boca Raton, 2014, p. 331-332.
44. F. Yang, W. Yang, Brittle versus ductile transition of nanocrystalline metals, International Journal of Solids and Structures 45 (2008) 3897-3907.
45. M. A. Meyers et al., Mechanical properties of nanocrystalline materials, Progress in Materials Science 51 (2006) 427-556.
46. B. K. Park et. al., Direct writing of copper conductive patterns by ink-jet printing, Thin Solid Films 515 (2007) 7706-7711.